Stress and displacement fields around an arbitrary shape tunnel surrounded by a multilayered elastic medium subjected to harmonic waves under plane strain conditions

Hamed Bouaré, Arnaud Mesgouez, Gaëlle Lefeuve-Mesgouez

To cite this version:

Hamed Bouaré, Arnaud Mesgouez, Gaëlle Lefeuve-Mesgouez. Stress and displacement fields around an arbitrary shape tunnel surrounded by a multilayered elastic medium subjected to harmonic waves under plane strain conditions. Soil Dynamics and Earthquake Engineering, 2022, 154, pp.107158. 10.1016/j.soildyn.2022.107158 . hal-03775952

HAL Id: hal-03775952
https://hal.inrae.fr/hal-03775952v1

Submitted on 22 Jul 2024

Stress and displacement fields around an arbitrary shape tunnel surrounded by a multilayered elastic medium subjected to harmonic waves under plane strain conditions

Hamed Bouare, Arnaud Mesgouez and Gaëlle Lefeuve-Mesgouez
UMR EMMAH, University of Avignon - INRAE
Campus Jean-Henri Fabre, Agroparc, 301 rue Baruch de Spinoza, BP 21239, 84916 Avignon cedex 9, France
Low Noise Inter-Disciplinary Underground Science and Technology, Rustrel, France

Abstract

This study focuses on the propagation of harmonic mechanical waves around both circular and non-circular tunnels. The excavation disturbed zone is explicitly modeled with a multilayered description of the surroundings of the tunnel. The purpose of this paper is thus to establish closed-form solutions for stress and displacement fields for circular and non-circular geometries taking into account the mechanical heterogeneity of the area adjacent to the tunnel. Particularly, the multilayered non-circular shape configuration is a great step not treated previously. The classical approach based on the wave function expansion method is used to determine the expressions of stresses and displacements around circular geometries. To handle non-circular tunnel shapes, the complex variable method based on the Muskhelishvili approach and conformal mapping functions is introduced. Results indicate that the excavation damaged zone strongly modifies the distribution of stress and displacement fields around the tunnel. Geometrical tunnel shapes also affect stress and displacement polar diagrams.

Keywords: Harmonic regime; Complex variable; Conformal mapping; Non circular tunnels; Semi-analytical model; Multilayered configurations

1 Introduction

Underground tunnels play an important role in mining, transportation industry and military engineering. Over the last decades, many techniques have been applied to detect and characterize underground facilities and their surroundings, including electrical, magnetic and mechanical methods. Seismic approaches are among the most successful for underground cavity detection. Priad and Piwakowski [1] proposed a high-resolution seismic reflection technique to localize and characterize French underground cavities at variable depths. Sloan et al. [2] presented work based on compressional wave diffraction and surface wave backscatter to detect a purpose-built subterranean tunnel. The tunneling industry has frequently assumed that tunnels are naturally resistant to earthquakes due to the traditional concept [3] and that underground facilities are less affected by seismic damage during earthquakes than structures on the ground surface. Large earthquakes have proven the opposite with significant seismic damage to underground structures [4]-[5]. Therefore, concrete linings have become the primary support to ensure the safety of underground structures. Several studies on tunnel strength have provided significant references for appropriate measurements, optimal design and safe operation of tunnels [6]-[9]. Also, excavation of underground tunnels affects the mechanical and hydraulic properties of the rock mass and the tunnel opening ultimately worsens the overall performance of the underground space. The Excavation Damage Zone (EDZ) is the failure zone due to stress redistribution induced by excavation and time depending on the behavior of the rock mass during blasting, drilling and mechanical excavation of the tunnel. Characterization of the disturbed zone is thus a very important task in the design and construction of deep underground tunnels, and for nuclear waste and natural gas storage applications, among others. The geometrical shapes of the tunnel and the EDZ can be varied, from quasi-cylindrical to horseshoe-shaped. Several authors have investigated the change of rock or soil properties due to the excavation disturbed zone: Kaewjuea and Senjuntichai [10] analyzed the influence of the excavation disturbed zone on the time-dependent response of a cylindrical borehole in a poroelastic medium; Meglis et al. [11] used ultrasonic wave velocity measurements to characterize the micro-crack population induced during the excavation of a tunnel at the Atomic Energy of Canada's Underground Research Laboratory; Tang et al. [12] used a coupled mechanical and a diffusion model to study the time-dependent development of the EDZ in a tunnel under high-humidity conditions; Zhoua et al. [13] proposed multilayered cylindrical

In this study, the primary goal is to provide semi-analytical solutions to determine stress and displacement fields around a non-circular tunnel with a multilayered description of the EDZ subjected to harmonic wave excitations. The work was carried out at the Low Noise Inter-Disciplinary Underground Science and Technology Laboratory (LSBB), an experimental environment located in southern France. The LSBB is characterized by a system of galleries, some of them presenting a concrete lining (Figure 1). The sub-horizontal galleries are 4 km long and are dug in a karstified limestone massif at a depth of 518 m in the heart of the unsaturated zone. In addition to the fractures generated during tunnel excavation, minor natural fractures are also present in the area of interest, J. Beres et al. [14].

In the literature on semi-analytical wave propagation in tunnels presenting a circular geometry, including potentially a multilayered approach for the lining of the tunnel with imperfect boundary conditions at the interfaces or for the EDZ, the historical works of Baron and Matthews [15] and Baron and Parnes [16] described the diffraction of pressure waves by a cylindrical cavity in an infinite elastic medium using integral transform method. Pao and Mow [17] studied the dynamic stress concentration factor of a circular tunnel in an elastic medium impacted by harmonic plane dilatational waves. Scorn [18] investigated the response of two-layered circular rod with imperfect bonding subjected to transient compressional waves. More recently, David et al. [19] proposed a Fourier–Bessel series development and a convex approximation of the half-space free surface to investigate the transverse response of underground cylindrical cavities subjected to incident shear (SV) waves. Esmaeili et al. [20] presented finite element and hybrid boundary methods to analyze the dynamic response of a lined circular tunnel subjected to harmonic plane waves. Lu et al. [21] investigated the dynamic stress concentration factor of the surrounding rock of a circular tunnel impacted by blasting dilatational cylindrical waves. Wang and Gong [22] studied the dynamic stresses in a multilayered cylinder subjected to dynamic pressure. On imperfect boundary conditions around the tunnel, Wang and Sudak [23] proposed a general method to study the scattering of elastic waves by multiple elastic circular cylinders with an imperfect interface. Yi et al. [24] and Shakeri et al. [25] also presented harmonic and transient approaches to analyze the response of a concrete tunnel with an imperfect contact embedded in an elastic rock, respectively.

Some researchers have studied non-circular lined and unlined tunnel geometries but without including a multilayered description of its surroundings. For example, Liu et al. [26] used the complex variable method to analyze the dynamic stress concentration factor around circular and elliptical cavities. Kargar et al. [27] presented an analytical solution for the stress field around a lined non-circular tunnel subjected to uniform ground load. Gerçek [28] presented an analytical solution for the elastic stress field occurring around tunnels or galleries with conventional shapes using a conformal mapping technique. Fang and Jin [29] used a visco-elastic interface model to investigate the dynamic stress field around a semi-circular and horseshoe-shaped lined tunnel subjected to harmonic compressional and shear waves. Zhao et al. [30] employed the complex variable method to find an analytical solution for rock stress around square tunnels in a homogeneous, isotropic and elastic rock mass. Hei et al. [31] proposed analytical solutions for elastic wave scattering by an arbitrary cavity in an in-homogeneous medium.

This study focuses on the propagation of harmonic mechanical waves around both circular and non-circular tunnels. The excavation disturbed zone is explicitly modeled with a multilayered description of the surroundings of the tunnel. The purpose of this paper is thus to establish closed-form solutions for stress and displacement fields for both circular and non-circular geometries, taking into account the mechanical heterogeneity of the area adjacent to the tunnel. Particularly, the multilayered non-circular shape configuration is a great step not treated previously. This paper is organized as follows: Section 2 describes accurate stress and displacement field solutions around a circular geometry. The concrete tunnel lining, the heterogeneous excavation disturbed zone and the surrounding limestone massif are assumed to be elastic and isotropic with various mechanical parameters. The mapping function theory with a complex variable approach is then used to transform a non-circular multilayered tunnel shape into a circular multilayered geometry for which analytical solutions could be developed. The study focuses on the assembly of the different layers in the two modelings underlining the differences and the key points to be cautious with. In Section 3, details of numerical computations and the results of stress and displacement fields around various tunnel shapes with a single or multilayered description of the EDZ are given. The mechanical input parameters are estimated using the ranges of density and velocities experimentally measured at the LSBB site. The results are analyzed by polar diagrams and show the influence of the tunnel and EDZ geometrical shapes on the hoop stress and radial displacement distributions.

The main steps to obtain the components of stress and displacement fields around a circular tunnel are described. The assembly process to handle the problem of a multilayered configuration to model the EDZ is explained. This section ends with a brief description of the complex variable method and the use of mapping functions to transform any kind of geometries into a circular shape. The assembly technique to deal with multilayered non-circular geometries is finally presented.

2.1 Positioning of the problem

The two-dimensional cross-section configuration is illustrated in Figure 2: a long tunnel is embedded in an infinite rock medium with a concrete lining. Due to the digging process, the area around the tunnel is weakened with the appearance of an EDZ. This zone is constituted by several layers around the lining assuming geometric regularity. The rock mass, the EDZ and the tunnel are considered as homogeneous, isotropic and elastic media. N_L defines the number of layers including the rock, the EDZ and the lining. For the circular or real geometry (right and left in the figure, respectively), η_k (resp. Ω_k) represents the rock mass medium when ($k = 1$), the lining medium when ($k = N_L$) and the damaged area is constituted of $N_L - 2$ layers ($k = 2, \ldots, N_L - 1$). Γ_k (resp. L_k) correspond to the different interfaces and the free surface ($k = N_L$). An incoming harmonic plane compressional wave with frequency ω and compressional wavenumber vector $\boldsymbol{\alpha_1}$ comes from the left side and propagates parallel to the x axis and perpendicular to the cross section of the tunnel.

In each medium under consideration, the displacement vector $\boldsymbol{u}$ is the solution of the Navier's elastodynamic equations. The usual gradient and curve decomposition of the displacement vector $\boldsymbol{u_k} = \nabla\phi_k + \nabla \times \boldsymbol{\Psi}_k$ is used, leading to the following Helmholtz equations

$$\nabla^2\phi_k - \frac{1}{c_{pk}^2}\ddot{\phi}_k = 0 \text{ and } \nabla^2\boldsymbol{\Psi}_k - \frac{1}{c_{sk}^2}\ddot{\boldsymbol{\Psi}}_k = \boldsymbol{0} \tag{1}$$

where ∇^2 indicates the Laplace operator, $c_{pk} = \sqrt{\frac{\lambda_k+2\mu_k}{\rho_k}}$, $c_{sk} = \sqrt{\frac{\mu_k}{\rho_k}}$ are the P and SV wave velocities in the elastic medium. λ_k, μ_k are the Lamé constants, ρ_k is the density and $(\ddot{\ })$ denotes double differentiation with respect to time.

2.2 Classical approach to solving the problem for circular geometries

The general method used to investigate the dynamic response of a layered circular tunnel is briefly summarized in this section. In the literature, many researchers analyzed the stress and displacement fields created around a circular cavity with or without lining. For instance, Pao and Mow [17] used the wave function expansion method to investigate the dynamic response of a circular tunnel in a homogeneous medium. Lee and Karl [35] gave a general formulation to study the scattering and diffraction of plane waves by underground, circular cavities at various depths. Wang et al. [36] studied the response of a tunnel in double-layered rocks subjected to compressional and shear harmonic waves. Zhao and Gary [37] proposed a three-dimensional analytical solution of the longitudinal wave propagation in an infinite linear viscoelastic cylindrical bar. More recently, Shakeri et al. [25] presented harmonic results analyzing the response of a concrete tunnel with an imperfect contact embedded in an elastic rock.

In this study on harmonic motion, the 2D total displacement potentials, indicated by exponent (T), in the **rock mass**, include incident and reflected waves and are given by

$$\phi_1^{(T)} = \sum_{n=0}^{\infty}[\varphi_0\epsilon_n i^n J_n(\alpha_1 r) + A_n H_n^{(1)}(\alpha_1 r)]\cos(n\theta) \text{ and } \psi_1^{(T)} = \sum_{n=0}^{\infty} B_n H_n^{(1)}(\beta_1 r)\sin(n\theta) \tag{2}$$

where $H_n^{(1)}$ is the Hankel function of the first kind of integer order n, $\beta_1 = \dfrac{\omega}{c_{s1}}$ is the shear wavenumber in the incident medium, and A_n and B_n are unknown coefficients corresponding to the modal expansion and to be determined based on the boundary conditions. Expression $\varphi_0 \sum_{n=0}^{\infty} \epsilon_n i^n J_n(\alpha_1 r)\cos(n\theta)$ corresponds to the incident wave expressed in terms of the Bessel-Fourier series, see Appendix A. The other terms correspond to reflected waves.

$$\phi_k^{(T)} = \sum_{n=0}^{\infty} [C_{nk} H_n^{(2)}(\alpha_k r) + D_{nk} H_n^{(1)}(\alpha_k r)] \cos(n\theta) \tag{3}$$

$$\psi_k^{(T)} = \sum_{n=0}^{\infty} [M_{nk} H_n^{(2)}(\beta_k r) + N_{nk} H_n^{(1)}(\beta_k r)] \sin(n\theta) \tag{4}$$

where k varies from 2 to N_L and identifies the layer under consideration, $H_n^{(2)}$ is the Hankel function of the second kind of an integer order n, and C_{kn}, M_{kn}, D_{kn} and N_{kn} are the unknown expansion coefficients per mode. The two incoming waves from the boundary are modeled by Hankel functions of the second kind $H_n^{(2)}$ and the two outgoing waves are written in terms of Hankel functions of the first kind $H_n^{(1)}$.

Displacement and stress components are linked to scalar and vector potentials ϕ and Ψ thanks to Helmholtz decomposition and behavior law, and are thus expressed with Hankel-Fourier series involving the unknown expansion coefficients.

Boundary and interface conditions respect the following : *(i)* perfect contact on each interface of the damaged area and between the EDZ and the mass rock; *(ii)* a free surface on the inner surface.

Combined with the use of the orthogonality properties of the trigonometric functions, it leads to the following matrix expression

$$\forall n \text{ (mode number)} \qquad [K]_{n,\{N_E,N_E\}} \{X\}_{n,N_E} = \{Y\}_{n,N_E} \tag{5}$$

and in a more detailed form

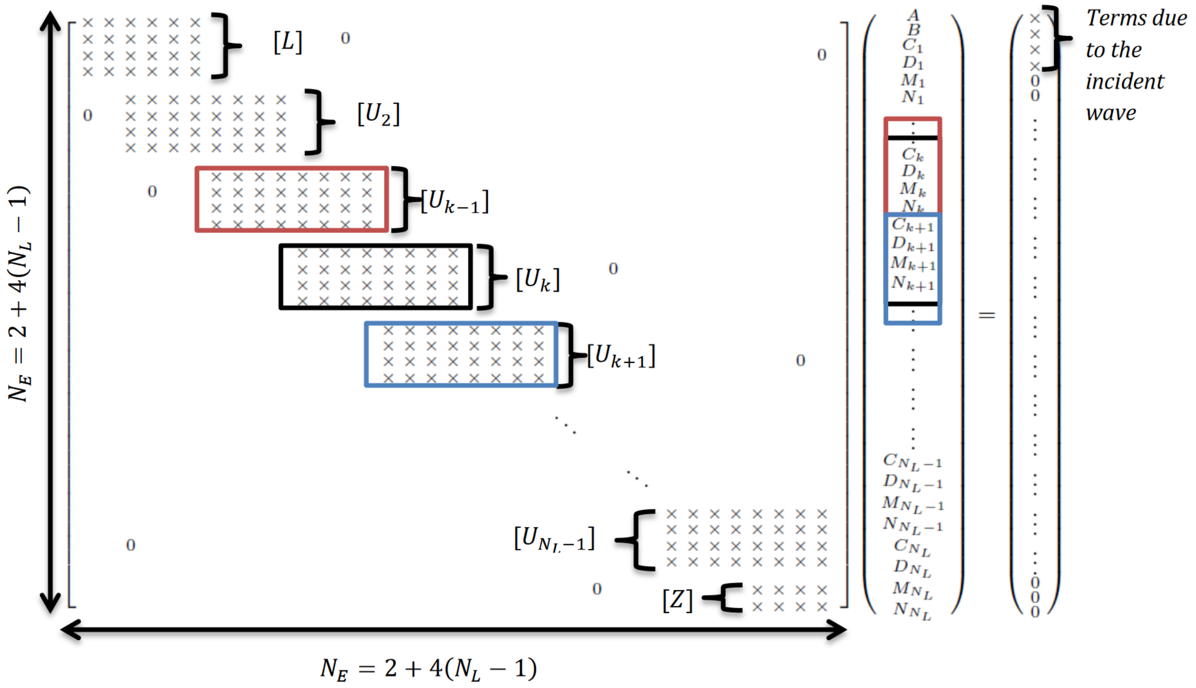

We omitted index n for the sake of clarify but $N_M (0 \leq n \leq N_M)$ systems are obtained

$\{X\}$ is a vector containing the unknown expansion coefficients per mode to be determined. $\{Y\}$ is a vector including the incident wave terms. They both have the dimension $N_E = 2 + 4(N_L - 1)$ where $N_L \geq 2$. $[K]$ is a square $N_E \times N_E$ matrix. The matrix $[K]$ is formed using the non zeros sub-matrices $[L]$, $[U_k]$ with $(k = 2, 3, ...N_L - 1)$ and $[Z]$. The first block $[L]$ is a 4×6 matrix and comes from writing the interface conditions on Γ_1. The last block $[Z]$ is a 2×4 matrix and takes into account the free surface conditions at the boundary Γ_{N_L}. $[U_k]$ is a repetitive block with a 4×8 dimension matrix coming from the interface obtained by summing the mode contributions. N_M therefore corresponds to truncation of the sums involved in the displacement and stress component expressions and must be chosen to achieve good convergence and results.

2.3 The complex function theory to solve the problem for more general geometries

In order to deal with the non circular shape of the tunnel, the complex variable method, explained by Liu et al. [26] for a tunnel embedded in an infinite homogeneous medium, is considered. The main characteristic of this method is to transform the real geometry into a cylindrical geometry to use the results developed for the cylindrical configuration and transform them to obtain the real displacement and stress fields. To do so, the real space is described by the complex variable $z = x + iy = \rho\, e^{i\chi}$ and transformed in a cylindrical geometry, also described by a complex variable $\eta = |\eta| e^{i\theta}$ with $\theta \in [0,\ 2\pi]$.

A conformal mapping function is used to transform each point of a unit circle into a point of the real interface and also each point outside the unit circle into a point outside the real interface. In the multilayered medium, each layer is transformed into a related layer in the real configuration (Figure 2). To simplify the approach, a unique mapping transform w is considered that transforms the free real surface (complex variable z) into a circular free surface (complex variable η). Then, all the interfaces are deduced from the same conformal mapping function.

According to Kargar et al. [27], Zhao and Yang [38] and, Fang and Jin [39], such a function $w(\eta)$ can be expressed as

$$w(\eta) = G\Big(\eta + \sum_{p=1}^{4} c_p \eta^{-p}\Big) \ \ with \ \ \eta = |\eta|\, \mathrm{e}^{i\theta}, \tag{6}$$

where G is the real parameter controlling the scale of the mapping function and coefficients c_p define the shape of geometry in the z-plane. Expressions $w(\eta_k)$ with the subscript $k = \{1, 2, \dots N_l\}$, describe more specifically the contours L_k. In order to obtain a single valued mapping function w and to avoid any self intersections at the interfaces, coefficients c_p must satisfy the following condition $0 \leq c_p \leq 1/p$. Choosing $c_p = 0$ provides a circle and choosing limiting values $c_p = 1/p$ gives a pore with $(p + 1)$ pointed cusps, [40] and [41].

The theoretical developments are based on [26] and [40], who considered only a tunnel embedded in an infinite medium without layering. The main steps of the method are briefly described omitting the intermediate developments. Introducing the conjugate complex variable $\overline{z}$ and derivatives related to complex variables z and $\overline{z}$, partial differential equations relative to Helmholtz potentials are expressed in the complex domain as

$$4\frac{\partial^2 \phi_k(z,\overline{z})}{\partial z \partial \overline{z}} + \alpha_k^2 \phi_k(z,\overline{z}) = 0 \tag{7}$$

$$4\frac{\partial^2 \psi_k(z,\overline{z})}{\partial z \partial \overline{z}} + \beta_k^2 \psi_k(z,\overline{z}) = 0 \tag{8}$$

Introducing a holomorphic function as described previously (such as relation 6) $z = w(\eta)$ and its conjugate form $\overline{z} = \overline{w(\eta)}$ and linking derivatives of z with respect to η and $\overline{z}$ with respect to $\overline{\eta}$, $\partial z = w'(\eta)\partial\eta$ and $\partial\overline{z} = \overline{w'(\eta)}\partial\overline{\eta}$, equations (7) and (8) are re-written in terms of variables η and $\overline{\eta}$

$$\frac{\partial^2 \phi_k(\eta,\overline{\eta})}{\partial \eta \partial \overline{\eta}} = \Big(\frac{i\alpha_k}{2}\Big)^2 w^{'}(\eta)\overline{w^{'}(\eta)}\phi_k(\eta,\overline{\eta}) \tag{9}$$

$$\frac{\partial^2 \psi_k(\eta,\overline{\eta})}{\partial \eta \partial \overline{\eta}} = \Big(\frac{i\beta_k}{2}\Big)^2 w^{'}(\eta)\overline{w^{'}(\eta)}\psi_k(\eta,\overline{\eta}) \tag{10}$$

Equations (9) and (10) must now be solved in the transformed circular geometry to obtain Helmholtz potentials.

The total displacement potentials of the **rock mass** are expressed as

$$\phi_1^{(T)}(\eta,\overline{\eta}) = \varphi_0 e^{i\alpha_1\Big(\frac{w(\eta)+\overline{w(\eta)}}{2}\Big)} + \sum_{n=-\infty}^{\infty} A_n H_n^{(1)}(\alpha_1|w(\eta)|)\Big[\frac{w(\eta)}{|w(\eta)|}\Big]^n \tag{11}$$

$n=-\infty$

These relations must be compared to those obtained in the classical cylindrical configuration. The main differences lie in the arguments of the Hankel functions since they now depend on the mapping function $w(\eta)$ and in the trigonometric functions replaced here by the ratio $\dfrac{w(\eta)}{|w(\eta)|}$.

The total displacement potentials in **the damaged area and the tunnel** are

$$\phi_k^{(T)}(\eta,\overline{\eta}) = \sum_{n=-\infty}^{\infty} \left\{ C_{kn} H_n^{(2)}(\alpha_k |w(\eta)|) + D_{kn} H_n^{(1)}(\alpha_k |w(\eta)|) \right\} \left[\frac{w(\eta)}{|w(\eta)|} \right]^n \tag{13}$$

$$\psi_k^{(T)}(\eta,\overline{\eta}) = \sum_{n=-\infty}^{\infty} \left\{ M_{kn} H_n^{(2)}(\beta_k |w(\eta)|) + N_{kn} H_n^{(1)}(\beta_k |w(\eta)|) \right\} \left[\frac{w(\eta)}{|w(\eta)|} \right]^n \tag{14}$$

As in the classical approach, a free surface on the lower boundary of the tunnel is considered, and the upper tunnel boundary and all other interfaces are assumed to be perfect.

The following n sets linear system of equations are expressed as

$$\{H\}_{n,N_E} = \{Q\}_{n,N_E} \tag{15}$$

Q contains the stress and displacement expressions of the incident wave in the rock mass, and H includes the stress and displacement relations of reflected and transmitted waves in all interfaces and boundaries. Due to the argument of the Hankel functions $\alpha_k|w(\eta)|$ and $\beta_k|w(\eta)|$, the orthogonality condition cannot be applied to equation (15). The unknown expansion coefficients can be determined from Fourier series expansion in a matrix formulation. As described in [26], [40] and [41], a periodic function Υ can be written in terms of the Fourier series

$$\Upsilon = \sum_{m=0}^{\infty} \Upsilon_m e^{im\theta} \quad \text{with} \quad \Upsilon_m = \frac{1}{2\pi} \int_0^{2\pi} \Upsilon e^{-im\theta} d\theta \tag{16}$$

where Υ_m is an expansion coefficient.

Applying the mathematical relation (16) to (15), a double Fourier series is obtained for both members of equation (15). The unknown expansion coefficients per mode become dependent on m and n, and the global linear system obtained as a function of mode is written

$$[G]_{n,m,\{M_E,M_E\}} \{P\}_{n,m,M_E} = \{I\}_{n,m,M_E}, \qquad m = n = 0, \pm 1, \pm 2, ... \pm N_M \tag{17}$$

where $[G]$ is a $(M_E \times M_E)$ coefficient matrix, $\{P\}$ and $\{I\}$ are the column vectors of size M_E. They are composed of the unknown expansion coefficients and the expressions due to the incident wave. As $M_E = (2N_M + 1) \times N_E$ is a function of N_M (number of modes), the dimensions of quantities $[G]$, $\{P\}$ and $\{I\}$ depend on the number of modes. The global matrix $[G]$ can be built using the sub-matrices $[R]$, $[V_k]$ with $(k = 2, 3, ...N_L - 1)$ and $[W]$ as presented in the following matrix system in concordance with Figure 3. The non-zeros block $[R]$ is a $4(2N_M + 1) \times 6(2N_M + 1)$ matrix and contains the contribution elements of stress and displacement at the interface $w(\eta_1)$. The non-zeros block $[W]$ is a $2(2N_M + 1) \times 4(2N_M + 1)$ matrix and includes the elements of stress at the boundary $w(\eta_{N_L})$. The non-zeros matrix $[V_k]$ with a $4(2N_M+1)\times 8(2N_M+1)$ dimension is a repetitive block and contains the elements of stress and displacement at the interfaces $w(\eta_2)$ to $w(\eta_{N_L-1})$. Each element noted by $[\times]$ in $[R]$, $[V_k]$ and $[W]$ is a $(2N_M+1)\times(2N_M+1)$ square matrix.

In the classical approach, the matrices and vectors obtained are independent on the number of modes N_M. In the complex variable approach, they are dependent on it and the same assembly algorithms cannot be used for both approaches. For a large number of modes, the global matrix $[G]$ can be huge.

3 Numerical results and discussion

3.1 Computational considerations and validation

Two Matlab codes have been developed to obtain the numerical results for the classical and complex approaches. For circular geometries, the arguments of the Hankel and Bessel functions in both methods are constant. However, for elliptical and horseshoe-shaped geometries, these arguments become variable and can lead to numerical oscillating features in the computation of these functions. A specific attention is needed at this stage. Several iterative solvers (GMRES, CGS, LSQR) have been tested during the numerical process to solve the global linear system obtained by both approaches and the BICGSTABL solver (Biconjugate Gradients Stabilized I Method) was ultimately chosen for its efficiency and accuracy. From a numerical point of view, the different numbers of modes used to obtain a good and reliable convergence of the Bessel-Fourier series for the circular and non-circular geometries are given in Table 3, Appendix B.

Two validation cases of the complex variable method for a multilayered configuration are proposed in this subsection. Firstly, our results are compared to those obtained by Liu et al. [26], who presented the results of the dynamic stress concentration factor for an elliptic cavity in a homogeneous infinite elastic plane subjected to a harmonic incident plane compressional wave. Rock, EDZ and lining are thus assumed here to be identical. The elastic half-space and the frequency content are directly chosen from the work by Liu et al. [26]. Figure 4 presents the dynamic stresses along the circumference of the elliptical cavity. Good agreement is found between the two sets of results. The expansion coefficients of the series obtained by both approaches are given in Table 4, Appendix B. The relative error is small. Differences may be due to computational performance and numerical accuracy since solvers and pre-conditioners have greatly evolved since the 1980s.

The second validation proposed in this work is a crosscheck between the usual and the complex variable approaches for a multilayered circular configuration. The mechanical parameters (density, P and S wave velocities) of each layer are given in Table 1 (case 3) and explained in section 3.2. Two incident frequencies are chosen: 200 Hz (called low frequency excitation) and 2 kHz (called high frequency excitation). The results are presented in a dimensionless form with the following notations

$$\sigma^*_{\theta\theta_k} = |\frac{\sigma_{\theta\theta_k}}{\sigma_0}|, \qquad \sigma^*_{rr_k} = |\frac{\sigma_{rr_k}}{\sigma_0}|, \qquad u^*_{r_k} = |\frac{u_{r_k}\zeta}{\varphi_0}| \tag{18}$$

where $\zeta = 1$ has the dimension of a distance (m). $\sigma_0 = \mu_1 \beta_1^2 \varphi_0$ denotes the stress intensity of the incident wave in the propagation direction.

Figure 5 shows the polar diagram of the hoop stress obtained by both approaches for the two chosen incident frequencies at the interface between the limestone and the first EDZ layer. Excellent agreement is obtained and allows the two approaches to be cross-checked.

	Incident	2800	5400	3300
Case 0 (black)	no EDZ			
Case 1 (magenta)	EDZ - Stiff (case 1)	2550	4400	2695
Case 2 (cyan)	EDZ - Soft (case 2)	2300	3450	2110
Case 3 (red)	EDZ 1 - Stiff (case 3)	2700	4800	2940
	EDZ 2 - Stiff (case 3)	2400	4000	2450
Case 4 (blue)	EDZ 1 - Soft (case 4)	2300	3700	2260
	EDZ 2 - Soft (case 4)	2300	3200	1960
	Concrete tunnel	2500	5031	2689

Table 1: Input data with a stiff layer (case 1), a soft layer (case 2), two stiff layers (case 3) and two soft layers (case 4) for modeling the EDZ. The mechanical parameters are estimated using the ranges of density and velocities experimentally measured at the LSBB site by [42] or [43].

Tunnel shape	$\lvert\eta_1\rvert$	$\lvert\eta_2\rvert$	$\lvert\eta_3\rvert$	$\lvert\eta_4\rvert$	G	c_1	c_2	c_3	c_4
Circular	3.4	2.9	2.4	2.0	0	0	0	0	0
Horizontal Elliptical	3.4	2.9	2.4	2.0	0.972	0.25	0	0	0
Horseshoe	1.413	1.20	0.995	0.82	$2.4e^{-i\frac{\pi}{2}}$	-0.01	-0.04	-0.002	-0.012

Table 2: Geometric coordinates and mapping coefficients of different tunnel shapes

3.2 Main results and discussion

In this work, the EDZ is modeled by one or two soft or stiff layers. The sets of mechanical values of each layer are presented in Table 1. The mechanical parameters are estimated using the ranges of density and velocities experimentally measured at the LSBB site by [42] or [43]. Soft and stiff values are related to the lowest and highest parts of the experimental intervals, respectively. The numerical results focus on two frequency ranges chosen as follows : a first low range related to a central frequency of the Ricker wavelet equals 200 Hz; this is the low frequency case and it corresponds to a wavelength around 20 m, thus 4 times the characteristic tunnel dimension. A second higher value, with a central frequency equal to 2 kHz, matches a wavelength around half the characteristic tunnel dimension. This choice can especially be justified because it corresponds to the wavelength or frequency ranges used in multifrequency inversion processes for parameter identification. Results proposed in this section concern the polar distribution of stress and displacement fields for:

- Case 0: Configuration for which only the lined tunnel embedded in a homogeneous limestone massif is considered (black lines).
- Cases 1 and 2: Description for which the EDZ is modeled with a single layer (magenta (stiff case) and cyan (soft case) lines). For the description, the mechanical parameters are the means chosen in the two-layer approach.
- Cases 3 and 4: Approach by which a two-layer model for the EDZ is used to describe more precisely the damaged zone around the tunnel (red (stiff case) and blue (soft case) lines).

The geometric coordinates and the mapping coefficients of the various tunnel shapes are presented in Table 2. Boundaries $w(\eta_1)$ and $w(\eta_2)$ correspond to the interfaces between the limestone massif and EDZ1, and between EDZ1 and EDZ2, respectively. Interfaces $w(\eta_3)$ and $w(\eta_4)$ describe the outer and inner tunnel boundaries.

3.2.1 Influence of the EDZ

Horizontal elliptical shape For an elliptical geometry, all results are symmetrical with respect to the horizontal axis, as expected. At low frequency (200 Hz) and for interface $w(\eta_1)$, the choice between single or two-layer modeling of the EDZ slightly affects the stress and displacement fields (Figures 6-7 on the left) since red and magenta curves are superposed as well as blue and cyan curves. The presence of a damaged area increases hoop stress (Figure 6) and radial displacement (Figure 7) for both stiff and soft cases. The

6-7 on the right). The choice of a multilayered description of the EDZ changes significantly the stress and displacement field polar diagrams. The maximum of hoop stress and radial displacement are obtained for stiff cases. Consequently, the effect of the EDZ is more significant for higher frequencies changing the order in the magnitudes and the field tendency.
Unlike interface $w(\eta_1)$, interface $w(\eta_3)$ shows, for a low frequency, a decrease of the hoop stress when considering the existence of the damaged area (Figures 8-9 left). Both interfaces $w(\eta_1)$ and $w(\eta_3)$ present slightly higher radial displacements when taking into account the EDZ. This is not the case for higher frequencies. The soft EDZ provides smaller hoop stress values and higher radial displacement values at low and high frequencies for $w(\eta_3)$. At interfaces $w(\eta_1)$ and $w(\eta_3)$, the hoop stress mean amplitude varies slightly with the frequency and large peaks are always observed between $\pi/6$ and $\pi/2$ (Figures 6 and 8). Concerning the radial displacement mean amplitudes (Figures 7 and 9), a notable increase in the frequency and the peak generally located at π is observed. Moreover, comparing Figures 6 and 8, when the EDZ is not taken into account (black curves), the amplitude increases at a low frequency whereas it remains of a similar order at a higher frequency. The order of magnitude is also greatly influenced by the frequency and the model chosen for the EDZ, but the impact is not similar for $w(\eta_1)$ and $w(\eta_3)$. Comparing Figures 7 and 9, radial displacement appear similar for one- or two-layer models for the low frequency, whereas they differ for the higher frequency. Consequently, the effect of the EDZ model is more visible for the higher frequency.

Horseshoe shape For a horseshoe-shaped tunnel, the stress and displacement field polar diagram shapes show differences in shape and amplitude compared to the ones obtained for the elliptical configuration, and all diagrams become non-symmetrical with respect to horizontal axis. As in the elliptical case, the results show that the presence of a damaged zone modifies the stress and displacement fields around the tunnel. At low and high frequencies, an increase in hoop stress and radial displacement is noted at the interface $w(\eta_1)$ when taking into account the EDZ (Figures 10-11). The soft EDZ provides the highest hoop stress and radial displacement values. Inside the massif at $w(\eta_3)$ and at a low frequency, the damaged zone increases slightly the radial displacement, and decreases the hoop stress component (Figures 12-13 left). At a high frequency, maximum large peaks situated around π appear for both the radial stress and the radial displacement components, and overall shapes of the polar diagrams become more disturbed (Figures 12-13 right). It is also important to notice that for both tunnel shapes (elliptical and horseshoe-shaped), the overall radial displacement fields increase with frequency, unlike the hoop stress field which decreases.

3.2.2 Influence of geometrical shape

This section studies the impact of geometrical shapes on the stress and displacement fields. The three shapes were chosen so that the geometrical points studied are rigorously the same for $\theta = 0$ and π, and very close elsewhere along the polar description. The case of two stiff-layer modeling of the EDZ is considered and the mechanical fields are plotted for $w(\eta_3)$ inside the massif. Figures 14-15 show that the geometrical shape considerably modifies the distribution of the stress and displacement components. At a low frequency, the polar diagrams for circular geometry are quite similar to those for the elliptic ones and quite different from the horseshoe-shaped configuration. At a high frequency, all diagrams show specific trends with a more dynamic overall response and a notable difference between the horseshoe-shaped and the circular-elliptic responses. The geometrical shapes are thus particularly important: in these results, the horseshoe-shaped case increases hoop stress and radial displacement around the galleries.

3.2.3 Frequency influence for different shapes

Figures 16-17 present the radial displacement obtained for the specific point $\theta = \pi$ at interface $w(\eta_3)$ for different geometries as a function of frequency over the range $[200 - 4500]$ Hz, including the limestone massif and the tunnel (case 0), and extensions to cases 3 and 4 where the damaged area is modeled with two stiff and soft layers. The main observations are as follows:

- For circular and elliptical shapes, the curves present an increasing behavior up to a maximum value and then decrease to a minimum value for a frequency between 3000 Hz and 3500 Hz (depending on the geometrical shape and the stiffness of the EDZ). Note that this value is close to the usual Rayleigh expression $f_0 = c_{p4}/4H$, (H is the thickness of the concrete layer), obtained in a 1D problem, [44]-[46]. This minimum is slightly shifted for the elliptical geometry. For the horseshoe shape, the same behavior is not observed.
- Oscillations appear when taking into account the EDZ, these are more perceptible in the soft case.

shaped geometry.

- All curves present another increasing behavior for frequencies above 3500 Hz, until a maximum value (not seen for all curves, depending on the chosen frequency range).
- Concerning the first maximum, it is obtained for lower frequency values when considering the EDZ. Moreover, the soft case presents two bumps (in addition to the oscillating feature) for both circular and elliptical configurations.

As an extension of this analysis, evolution of the radial displacement was investigated at interface $w(\eta_3)$ and $\theta = \pi$ as a function of the incident frequency for various thicknesses of the concrete layer in case of circular and elliptical geometries. It confirms that the position of the minimum in the circular case is obtained for $f_0 = c_{p4}/4H$. Specifically, the following is obtained: pink curve, $H = 0.8$ yields $f_0 = 1572$ Hz, cyan curve, $H = 0.7$ yields $f_0 = 1797$ Hz, red curve $H = 0.6$ yields $f_0 = 2096$ Hz, and so on. The oscillations appearing when taking into account the EDZ are quite similar when comparing curves with different thicknesses. A specific change occurs for the second increasing part of the curves: they present a greater slope at the beginning and for the same value of frequency for all cases studied (around 3150 Hz), and then the secondary oscillations are achieved (Figures 18-20).

4 Conclusion

In this work, the complex variable method was used to determine and analyze the stress and displacement fields induced by a harmonic plane wave around circular, elliptical and horseshoe-shaped concrete tunnels, including a multilayered radial description of the excavation damaged zone. The mapping function concept transforms a real configuration to a circular one. The main difference between the usual approach for circular geometries and the complex variable approach for more various geometries lies in the argument of the Hankel and Bessel functions that are no longer constant in the latter case. The work specifically focused on the multilayered aspect of the EDZ and the associated assembling process. Coupling of both a non-circular geometry and a multilayered configuration of the ground is a great advance for semi-analytical works. The results were validated in two different ways: comparison with literature results and comparison between the usual method in the case of circular geometries. The mechanical input parameters used in this work were directly estimated using the ranges of density and velocities experimentally measured at the LSBB site. The presence of the damaged zone changes the stress and displacement fields around the tunnel. The geometrical tunnel shapes also affect the stresses and displacements polar diagrams. For circular or elliptical configurations, all results are symmetrical with respect to the horizontal axis as opposed to the horseshoe shape where they become asymmetrical. Study of the influence of the EDZ in terms of both multilayered and shaped models has been proposed. Moreover, analysis of the load frequency and the lining thickness shows resonant behavior for a specific combination. In the near future, this approach will be extended to porous media to improve the model and include the fluid influence on the behavior. Study of the contact between the different layers taking into account imperfect contact will also be included in the model to better describe the potential fractures between two successive layers.

5 Acknowledgements

This work was carried out under a PhD grant from Conseil Général Provence-Alpes-Cote d'Azur, France. This support is gratefully acknowledged.

References

[1] L. Driad, B. Piwakowski, Detection and characterisation of underground cavities using high resolution seismic reflection (HRSR), Environ. Eng. Geophys. (2002) 31-34. https://doi.org/10.3997/2214-4609.201406148

[2] S.D. Sloan, S.L. Peterie, R.D. Miller, J. Ivanov, J.R. McKenna, S.W. Broadfoot, O.M. Metheny, Tunnel detection using near-surface seismic methods, SEG Technical Program Expanded Abstracts 1-5 2012. https://doi.org/10.1190/segam2012-1442.1

[3] T. Ikuo, Geotechnical Earthquake Engineering, Springer, Berlin, Germany 2008.

0367-6

[5] G. Tsinidis, F. de Silva, I.Anastasopoulos, E. Bilotta A. Bobet, Y.M.A. Hashash, C. He, G. Kampas, J. Knappett, G. Madabhushi, N. Nikitas, K. Pitilakis, F. Silvestri, G. Viggiani, R. Fuentes, Seismic behaviour of tunnels: From experiments to analysis, Tunn. Undergr. Space Technol. 99 (2020) 103 334. https://doi.org/10.1016/j.tust.2020.103334

[6] R. Hölter, C. Zhao, E. Mahmoudi, A.A. Lavasan, M. Datcheva, M. König, T. Schanz, Optimal measurement design for parameter identification in mechanized tunneling, Undergr. Space 3 (2018) 34-44. https://doi.org/10.1016/j.undsp.2018.01.004

[7] S. Pelizza, Pilot bore excavation with TBM for the design and construction of larger tunnels, Tunn. Undergr. Space Technol. 6 (1991) 185–189. https://doi.org/10.1016/0886-7798(91)90065-C

[8] H. Fazli, Optimal design of tunnel support lining using MCBO algorithm, Int. J. Optim. Civil Eng. 7 (2017) 339-354. http://ijoce.iust.ac.ir/article-1-301-en.html

[9] P.K. Swamee, B.N. Asthana, Optimal design of a power tunnel, J. Hydraul. Eng. 19 (2013) 21-26. https://doi.org/10.1080/09715010.2012.742288

[10] W. Kaewjuea, T. Senjuntichai, Poromechanical response of borehole in excavation disturbed zone, Comput. Geotech. 56 (2014) 148-159. https://doi.org/10.1016/j.compgeo.2013.12.002

[11] L.L. Meglis, T. Chow, R.P. Young, Assessing microcrack damage around a tunnel at the underground research laboratory using ultrasonic velocity tomography, Thirty-Eighth Rock Mechanics Symposium, DC Rocks, Washington DC, USA 919–925 2001.

[12] S. Tang, C. Yu, C. Tang, Numerical modeling of the time-dependent development of the damage zone around a tunnel under high humidity conditions, Tunn. Undergr. Space Technol. 76 (2018) 48–63. https://doi.org/10.1016/j.tust.2018.03.012

[13] F. Zhoua, Z. Songa, C. Lin, Hydromechanical behavior of radially multilayered cylinders under time-varying loads, Mar. Georesour. Geotechnol. 37 (2019) 506–516. https://doi.org/10.1080/1064119X.2017.1412549

[14] J. Beres, H. Zeyen, G. Sénéchal, D. Rousset, S. Gaffet, Seismic anisotropy analysis at the Low-Noise Underground Laboratory (LSBB) of Rustrel (France), J. Appl. Geophys. 94 (2013) 59-71. https://doi.org/10.1016/j.jappgeo.2013.04.008

[15] M.L. Baron, A. Matthews, Diffraction of a pressure wave by a cylindrical cavity in a elastic medium, J. Appl. Mech. 28 (1961) 347–354. https://doi.org/10.1115/1.3641710

[16] M.L. Baron, R. Parnes, Displacements and velocities produced by the diffraction of a pressure wave by a cylindrical cavity in an elastic medium, J. Appl. Mech. 29 (1962) 385-395. https://doi.org/10.1115/1.3640559

[17] Y.H. Pao, C.C. Mow, Diffraction of elastic waves and dynamic stress concentrations, Rand, Crane Russak, New York, 681 pages, 1971.

[18] R.A. Scorn, Transient compressional wave propagation in a two-layered circular rod with imperfect bonding, J. Sound Vib. 26 (1973) 321–335. https://doi.org/10.1016/S0022-460X(73)80188-9

[19] C.A. Davis, V.W. Lee, J.P. Bardet, Transverse response of underground cavities and pipes to incident SV waves, Earthq. Eng. Struct. Dyn. 30 (2001) 383–410. https://doi.org/10.1002/eqe.14

[20] M. Esmaeili, S. Vahdani, A. Noorzad, Dynamic response of lined circular tunnel to plane harmonic waves, Tunn. Undergr. Space Technol. 21 (2006) 511–519. https://doi.org/10.1016/j.tust.2005.10.002

[21] Shiwei Lu, C. Zhou, Z. Zhang, N. Jiang, Dynamic stress concentration of surrounding rock of a circular tunnel subjected to blasting cylindrical P-Waves, J. Geotech. Geol. Eng. 37 2363–2371 2019. https://doi.org/10.1007/s10706-018-00761-5

[22] X.Wang, Y.N.Gong, An elastodynamic solution for multilayered cylinders, Int. J. Eng. Sci. 30 (1992) 25-33. https://doi.org/10.1016/0020-7225(92)90118-Z

https://doi.org/10.1080/17455030601118376

[24] C.P. Yi, W.b. Lu, P. Zhang, D. Johansson, U. Nyberg, Effect of imperfect interface on the dynamic response of a circular lined tunnel impacted by plane P-waves, Tunn. Undergr. Space Technol. 21 (2016) 68-74. https://doi.org/10.1016/j.tust.2015.10.011

[25] R. Shakeri, A. Mesgouez, G. Lefeuve-Mesgouez, Transient response of a concrete tunnel in an elastic rock with imperfect contact, Int. J. Min. Sci. Technol. 30 (2020) 605-612. https://doi.org/10.1016/j.ijmst.2020.05.008

[26] D. Liu, B. Gai, G. Tao, Applications of the method of complex functions to dynamic stress concentrations, Wave Motion 4 (1982) 293-304. https://doi.org/10.1016/0165-2125(82)90025-7

[27] A.R. Kargar, R. Rahmannejad, M.A. Hajabasi, A semi-analytical elastic solution for stress field of lined non-circular tunnels at great depth using complex variable method, J. Solids Struct. 51 (2014) 1475–1482. https://doi.org/10.1016/j.ijsolstr.2013.12.038

[28] H. Gerçek, An elastic solution for stresses around tunnels with conventional shapes, Int. J. Rock Mech. Min. Sci. 34 (1997) 3–4. https://doi.org/10.1016/S1365-1609(97)00091-9

[29] X.Q. Fang, H.X. Jin, Visco-elastic imperfect bonding effect on dynamic response of a non-circular lined tunnel subjected to P and SV waves, Soil Dyn. Earthq. Eng. 88 (2016) 1–7. https://doi.org/10.1016/j.soildyn.2016.05.014

[30] G. Zhao, S. Yang, Analytical solutions for rock stress around square tunnels using complex variable theory, Int. J. Rock Mech. Min. Sci. 80 (2015) 302–307. https://doi.org/10.1016/j.ijrmms.2015.09.018

[31] B. Hei, Z. Yang, Y. Wang, D. Liu, Dynamic analysis of elastic waves by an arbitrary cavity in an inhomogeneous medium with density variation, J. Math. Mech. Solids 21 (2016) 931-940. https://doi.org/10.1177/1081286514545906

[32] H. Garnet, J.C. Pascal, Transient Response of a Circular Cylinder of Arbitrary Thickness in an Elastic Medium to a Plane Dilatational Wave, J. Appl. Mech. 33 (1966) 521-531. https://doi.org/10.1115/1.3625117

[33] A. Wirgin, Retrieval of the equivalent acoustic constitutive parameters of an inhomogeneous fluid-like object by nonlinear full waveform inversion, Ultrasonics 65 (2016) 353–369. https://doi.org/10.1016/j.ultras.2015.09.005

[34] C.C. Mei, Wave propagation, MIT course (2004). http://hdl.handle.net/1721.1/41865

[35] V.W Lee, J Karl, Diffraction of SV waves by underground, circular, cylindrical cavities, Soil Dyn. Earthq. Eng. 11 (1992) 445-456. https://doi.org/10.1016/0267-7261(92)90008-2

[36] T.T. Wang, J.T Hsu, C.H Chen, T.H. Huang, Response of a tunnel in double layer rocks subjected to harmonic P and S waves, Int. Rock Mech. Min. Sci. 70 (2014) 435–443. https://doi.org/10.1016/j.ijrmms.2014.06.002

[37] H. Zhao, G. Gary, A Three Dimensional Analytical Solution of the longitudinal wave Propagation in an infinite Linear viscoelastic cylindrical Bar, Application to Experimental Techniques, J. Mech. Phys. Solids 43 (1995) 1335-1348. https://doi.org/10.1016/0022-5096(95)00030-M

[38] G. Zhao, S. Yang, Analytical solutions for rock stress around square tunnels using complex variable theory, Int. J. Rock Mech. Min. Sci. 80 (2015) 302–307. https://doi.org/10.1016/j.ijrmms.2015.09.018

[39] X.Q. Fang, H.X. Jin, Dynamic response of a non-circular lined tunnel with visco-elastic imperfect interface in the saturated poroelastic medium, Comput. Geotech. 83 (2017) 98-105. https://doi.org/10.1016/j.compgeo.2016.11.001

[40] N.I. Muskhelishvili, Some Basic Problems of the Mathematical Theory of Elasticity, trans. From 4^{th} Edn (in Russian) by J.R.M. Radok, University of Groningen, Netherlands, Noordhoff, New York 1963.

[41] G. Liu, P.G. Jayathilake, B.C. Khoo F. Han, D. Liu, Conformal mapping for the Helmholtz equation: Acoustic wave scattering by a two dimensional inclusion with irregular shape in an ideal fluid, J. Acoust. Soc. Am. 1433 (2012) 43-46. https://doi.org/10.1063/1.3703135

Geol. 44 (2012) 93-109. https://doi.org/10.1016/j.jsg.2012.08.016

[43] L. Duboeuf, Injections de fluide dans une zone de faille (LSBB, Rustrel) : sismicité induite et déformation asismique, Ph.D. Thesis (in French), Université Côte d'Azur (2018). https://tel.archives-ouvertes.fr/tel-01787649

[44] L. Flax, G.G Gaunaurd, H. Uberall, Theory of resonance scattering, Phys. Acoust. 15 (1981) 191-294. https://doi.org/10.1016/B978-0-12-477915-0.50008-7

[45] D. Brill, G. Gaunaurd, Resonance theory of elastic waves ultrasonically scattered from an elastic sphere, J. Acoust. Soc. Am. 81 (1987) 1-21. https://doi.org/10.1121/1.394983

[46] A.J. Haug, S.G. Solomon, H. Überall, Resonance theory of elastic wave scattering from a cylindrical cavity, J. Sound Vib. 57 (1978) 51-58. https://doi.org/10.1016/0022-460X(78)90279-1

[47] J.B. Martino, N.A. Chandler, Excavation-induced damage studies at the underground research laboratory, Int. J. of Rock Mech. Min. Sci. 41 (2004) 1413-1426. https://doi.org/10.1016/j.ijrmms.2004.09.010

[48] P. Blümling, F. Bernier, P. Lebon, C.D Martin, The excavation damaged zone in clay formations time-dependent behaviour and influence on performance assessment, Phys. Chem. Earth 32 (2007) 588-599. https://doi.org/10.1016/j.pce.2006.04.034

[49] J.B. Martino, N.A. Chandler, Excavation-induced damage studies at the underground research laboratory. Int. J. Rock Mech. Min. Sci. 41 (2004) 1413–1426. https://doi.org/10.1016/j.ijrmms.2004.09.010

[50] F. Pellet, M. Roosefid, F. Deleruyelle, On the 3D numerical modelling of the time dependent development of the damage zone around underground galleries during and after excavation, Tunn. Undergr. Space Technol. 24 (2009) 665–674. https://doi.org/10.1016/j.tust.2009.07.002

6.1 Appendix A : expressions for incident waves

Cylindrical tunnel shape case

Following the usual methodology proposed by Pao and Mow [17], Garnet and Pascal [32] and Wirgin [33], among others, the incident scalar potential is expressed as follows (incident denoted as an exponent "(i)")

$$\phi^{(i)} = \varphi_0 \, \mathrm{e}^{i\alpha_1 r \cos\theta} \tag{19}$$

where φ_0 is the amplitude of the scalar potential of the incident wave, α_1 is the incident compressional wavenumber and (r,θ) corresponds to the polar coordinates. The frequency dependency is omitted to make reading easier.

Based on the expansion method [34], the incident wave is expressed in terms of the Bessel-Fourier series as

$$\phi^{(i)} = \varphi_0 \sum_{n=0}^{\infty} \epsilon_n i^n J_n(\alpha_1 r) \cos(n\theta) \tag{20}$$

where J_n is the Bessel function of the first kind of an integer n and ϵ_n is the Jacobi symbol.
$\epsilon_n = 1$ for $n = 0$ and $\epsilon_n = 2$ for $n > 0$.

General tunnel shape case

The time-harmonic incident compressional plane wave that propagates perpendicular to the tunnel cross section is expressed in the complex domain as

$$\phi^{(i)}(\eta, \overline{\eta}) = \varphi_0 e^{i\alpha_1 x} = \varphi_0 e^{i\alpha_1 \left(\dfrac{z+\overline{z}}{2}\right)} = \varphi_0 e^{i\alpha_1 \left(\dfrac{w(\eta)+\overline{w(\eta)}}{2}\right)} \tag{21}$$

Tunnel shapes	Interface	Frequencies (Hz)	Total Number of modes $N_M + 1$ / $2N_M + 1$
Circular (classical and complex approaches)	$w(\eta_1)$	200	5/9
Circular (classical and complex approaches)	$w(\eta_1)$	2000	21/31
Horizontal Elliptical	$w(\eta_1)$, $w(\eta_3)$	200	15
Horizontal Elliptical	$w(\eta_1)$, $w(\eta_3)$	2000	31
Horseshoe	$w(\eta_1)$, $w(\eta_3)$	200	13
Horseshoe	$w(\eta_1)$, $w(\eta_3)$	2000	31

Table 3: Number of modes necessary for the convergence of the Bessel-Fourier series (circular/non-circular geometries). In the classical approach, since the Bessel Fourier series ranges from 0 to N_M, the total number of modes corresponds to $N_M + 1$. In the complex variable approach, it is equal to $2N_M + 1$.

Expansion coefficients	H. Bouare et al.	D. Liu et al. [26]	Relative error
A_{-3}	$-0.408951 \times 10^{-4} + i0.105877 \times 10^{-5}$	$-0.409825 \times 10^{-4} + i0.101251 \times 10^{-5}$	0.0024
A_{-2}	$0.588472 \times 10^{-3} - i0.6638459 \times 10^{-2}$	$0.588153 \times 10^{-3} - i0.664517 \times 10^{-2}$	0.0010
A_{-1}	$-0.9821807 \times 10^{-2} + i0.390646 \times 10^{-3}$	$-0.981691 \times 10^{-2} + i0.391336 \times 10^{-3}$	0.0005
A_0	$-0.111208 \times 10^{-2} + i0.374542 \times 10^{-1}$	$-0.111462 \times 10^{-2} + i0.314570 \times 10^{-1}$	0.1905
A_1	$0.982181 \times 10^{-2} - i0.390645 \times 10^{-3}$	$0.981380 \times 10^{-2} - i0.394345 \times 10^{-3}$	0.0009
A_2	$0.588472 \times 10^{-3} - i0.663845 \times 10^{-2}$	$0.588029 \times 10^{-3} - i0.664492 \times 10^{-2}$	0.0010
A_3	$0.4089506 \times 10^{-4} - i1.058771 \times 10^{-6}$	$0.409887 \times 10^{-4} - i0.990927 \times 10^{-6}$	0.0028
B_{-3}	$-0.547375 \times 10^{-5} - i0.211882 \times 10^{-3}$	$-0.523445 \times 10^{-5} - i0.212331 \times 10^{-3}$	0.0024
B_{-2}	$0.198677 \times 10^{-1} + i0.175602 \times 10^{-2}$	$0.198875 \times 10^{-1} + i0.175506 \times 10^{-2}$	0.0010
B_{-1}	$-0.670366 \times 10^{-3} - i0.171018 \times 10^{-1}$	$-0.671594 \times 10^{-3} - i0.170935 \times 10^{-1}$	0.0005
B_0	$4.446479 \times 10^{-14} + i1.3040109 \times 10^{-14}$	$-0.386065 \times 10^{-6} - i0.595808 \times 10^{-6}$	1.0000
B_1	$-0.670366 \times 10^{-3} - i0.171018 \times 10^{-1}$	$-0.676553 \times 10^{-3} - i0.170881 \times 10^{-1}$	0.0009
B_2	$-0.198677 \times 10^{-1} - i0.001756 \times 10^{-2}$	$-0.198867 \times 10^{-1} - i0.175470 \times 10^{-2}$	0.0870
B_3	$-0.547376 \times 10^{-5} - i0.211882 \times 10^{-3}$	$-0.512241 \times 10^{-5} - i0.212365 \times 10^{-3}$	0.0028

Table 4: Comparison between expansion coefficients with Liu et al. [26] for an elliptical geometry with $\alpha a = 0.20$ and $a/b = 3/2$.


Tunnel
Main kilometric faults
Secondary faults
N
0
200 m
Blinded capsule
Main gallery
Emergency exit
Anti-blast gallery
Entry
LSBB

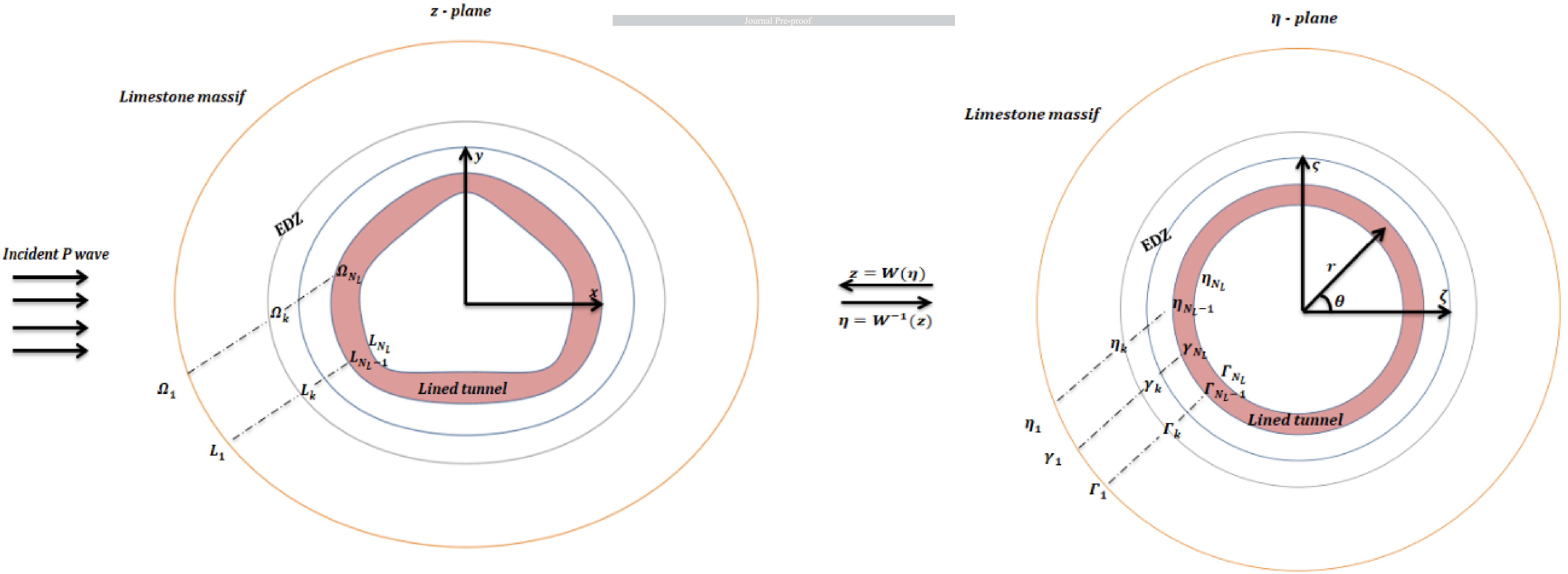
z - plane
Limestone massif
EDZ
Incident P wave
y
x
Ω_{N_L}
Ω_k
Ω_1
L_{N_L}
L_{N_L-1}
L_k
L_1
Lined tunnel
$z = W(\eta)$
$\eta = W^{-1}(z)$
η - plane
Limestone massif
EDZ
ς
ζ
r
θ
η_{N_L}
η_{N_L-1}
η_k
η_1
γ_{N_L}
γ_k
γ_1
Γ_{N_L}
Γ_{N_L-1}
Γ_k
Γ_1
Lined tunnel

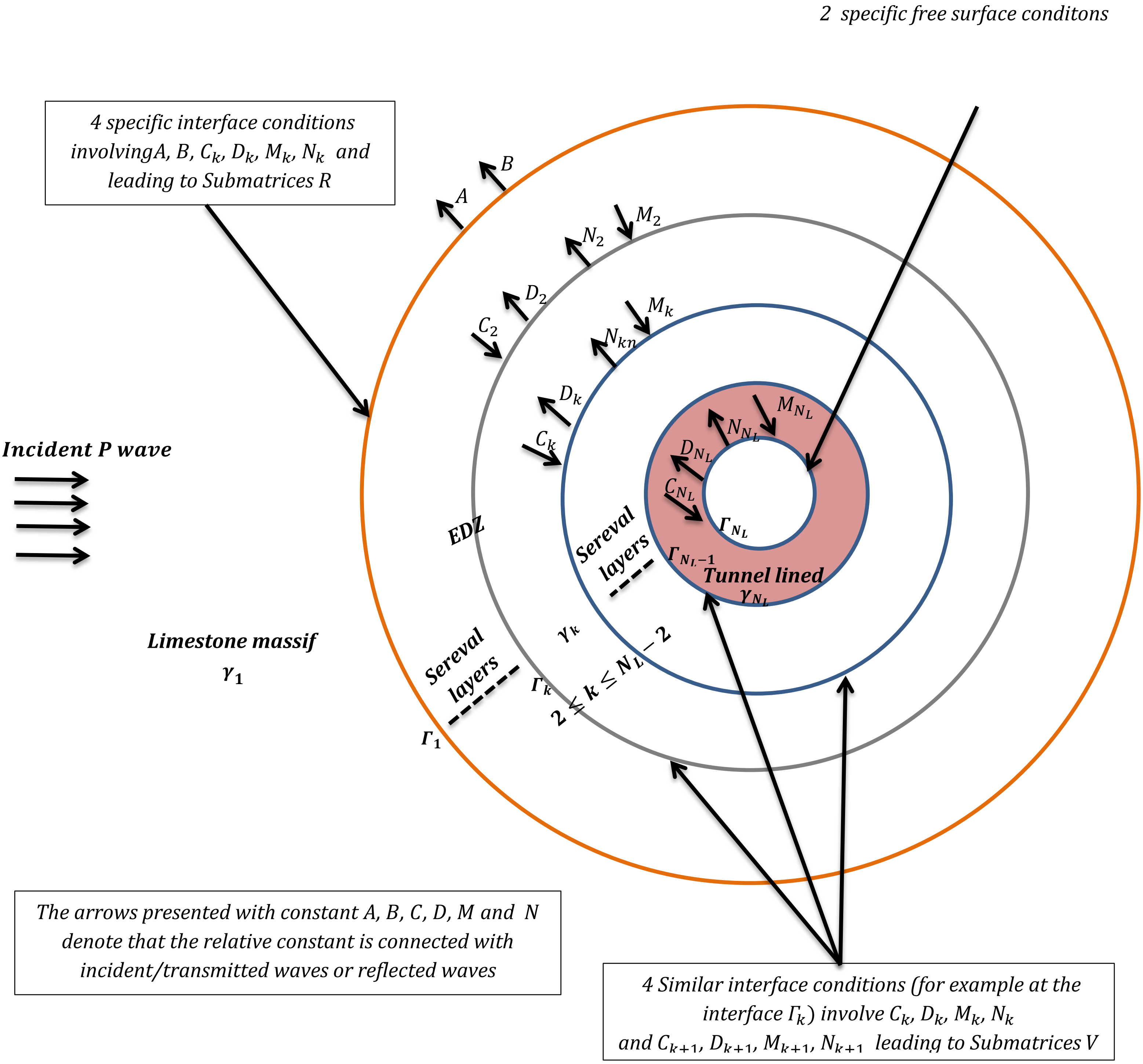

2 specific free surface conditons

4 specific interface conditions involving$A$, B, C_k, D_k, M_k, N_k and leading to Submatrices R

The arrows presented with constant A, B, C, D, M and N denote that the relative constant is connected with incident/transmitted waves or reflected waves

4 Similar interface conditions (for example at the interface Γ_k) involve C_k, D_k, M_k, N_k and C_{k+1}, D_{k+1}, M_{k+1}, N_{k+1} leading to Submatrices V

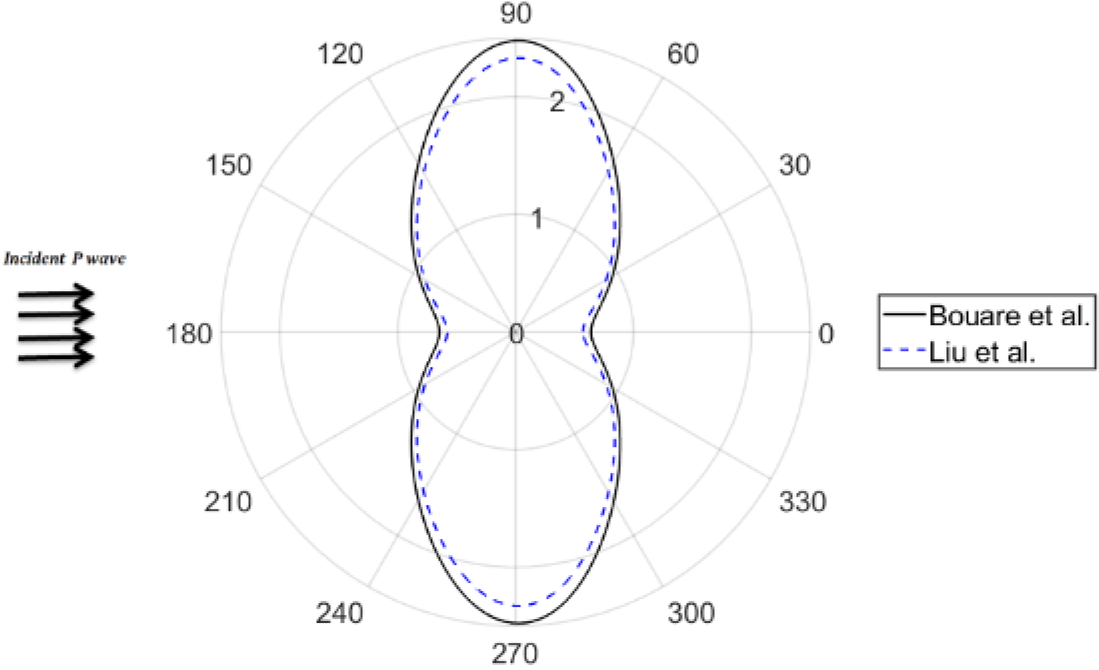
90
120
60
150
30
2
1
0
Incident P wave
180
0
Bouare et al.
Liu et al.
210
330
240
300
270

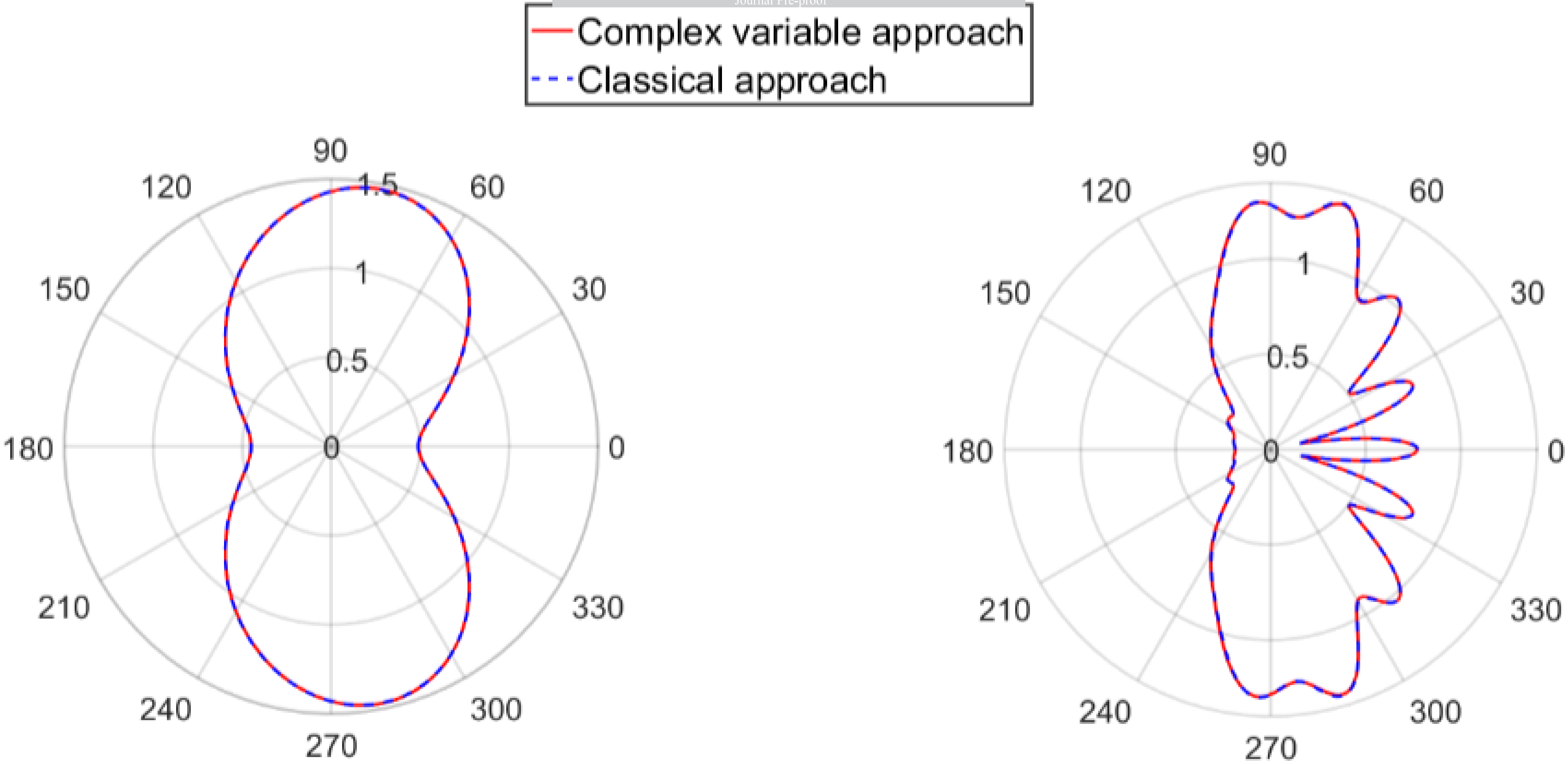
Complex variable approach
Classical approach
90
120
60
150
30
180
0
210
330
240
300
270
1.5
1
0.5
0
90
120
60
150
30
180
0
210
330
240
300
270
1
0.5
0

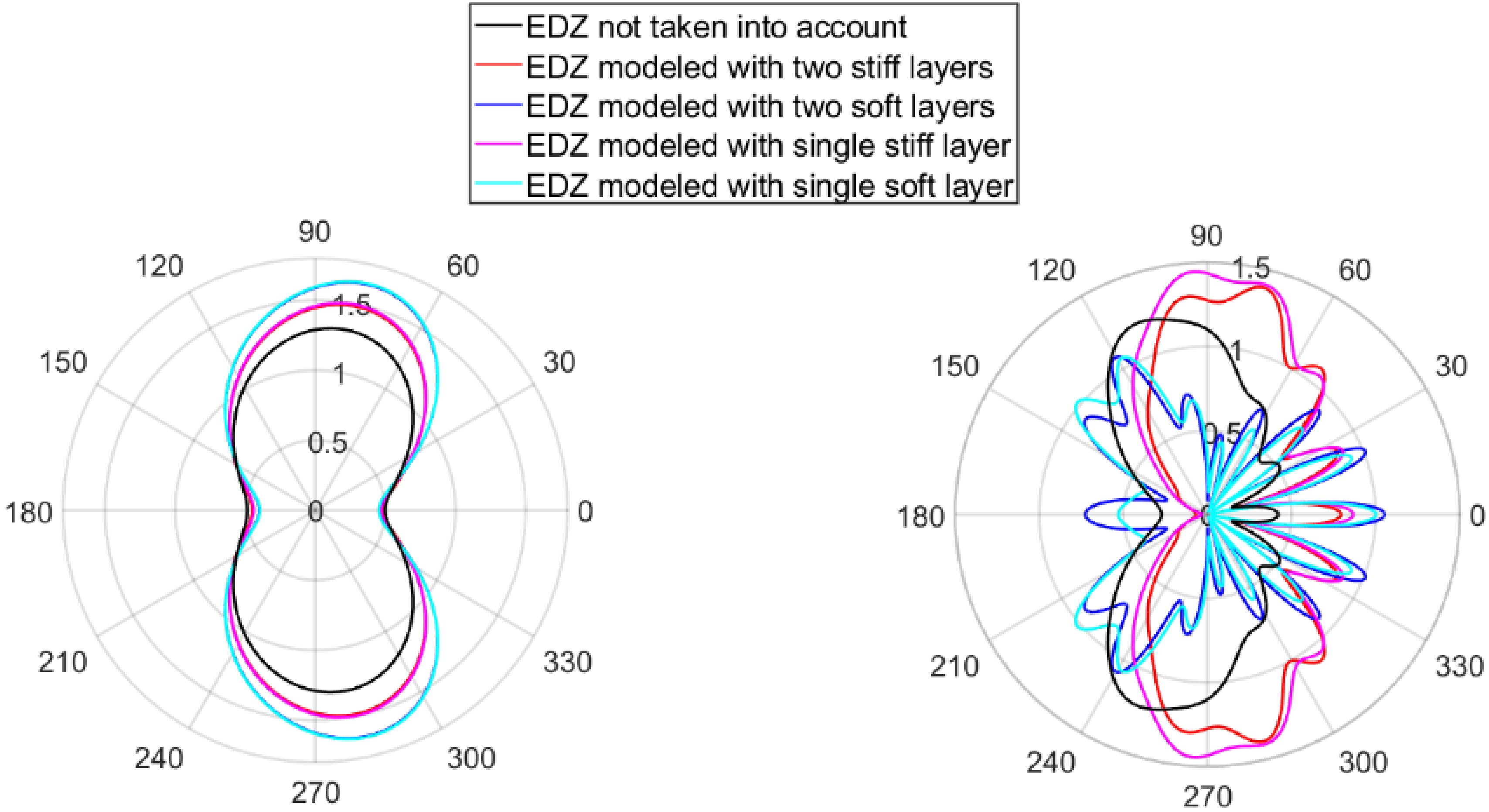
EDZ not taken into account
EDZ modeled with two stiff layers
EDZ modeled with two soft layers
EDZ modeled with single stiff layer
EDZ modeled with single soft layer
90
120
60
150
30
180
0
210
330
240
300
270
0
0.5
1
1.5
90
120
60
150
30
180
0
210
330
240
300
270
0
0.5
1
1.5

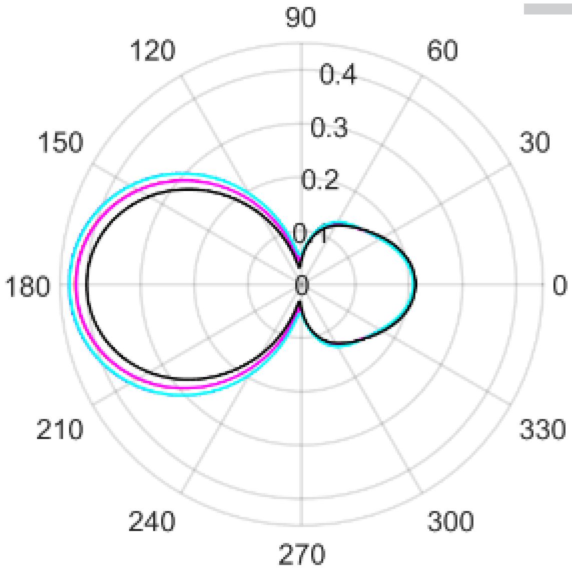
90
120
60
0.4
0.3
150
30
0.2
0.1
180
0
0
210
330
240
300
270

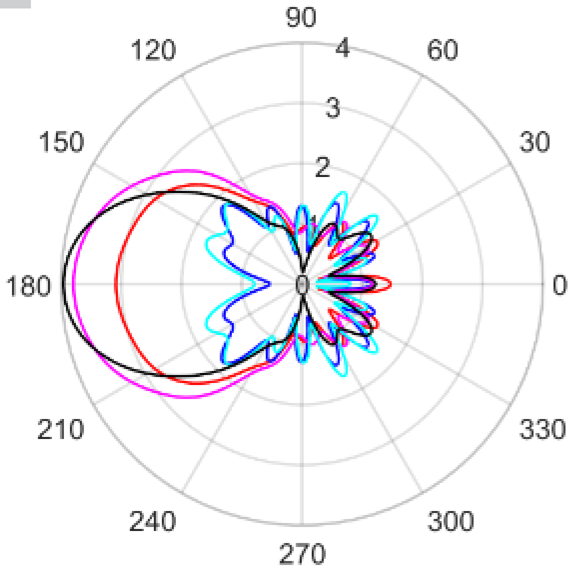
90
4
120
60
3
150
30
2
1
180
0
0
210
330
240
300
270

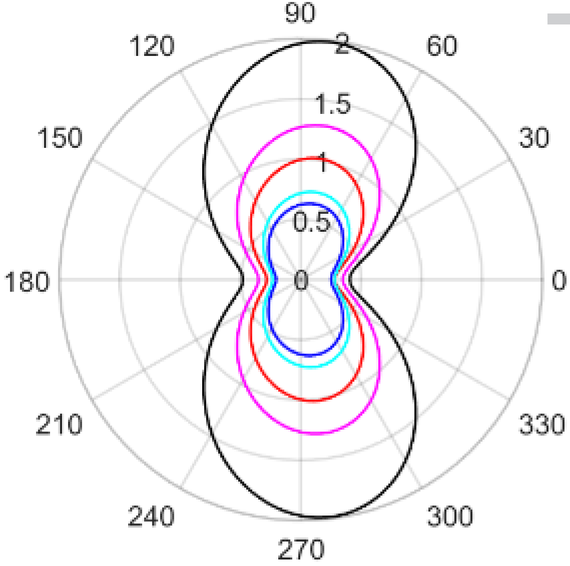
90
120
60
150
30
180
0
210
330
240
300
270
2
1.5
1
0.5
0

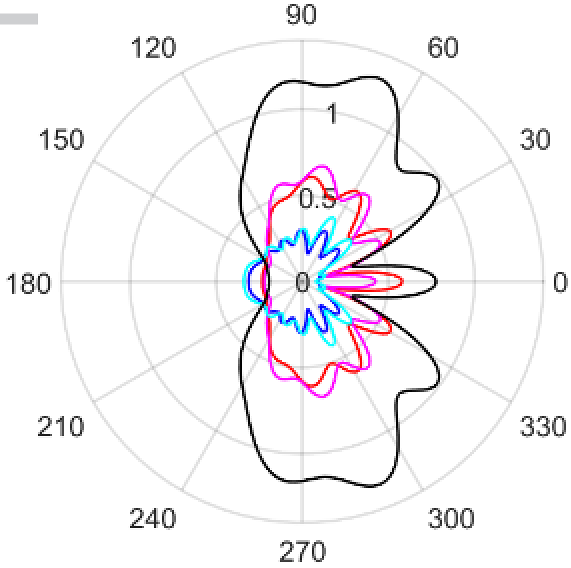
90
120
60
150
30
180
0
210
330
240
300
270
1
0.5
0

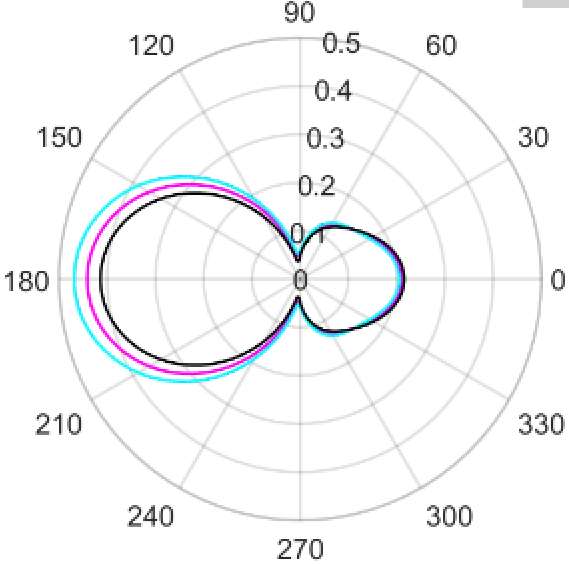
90
120
60
150
30
180
0
210
330
240
300
270
0.5
0.4
0.3
0.2
0.1
0

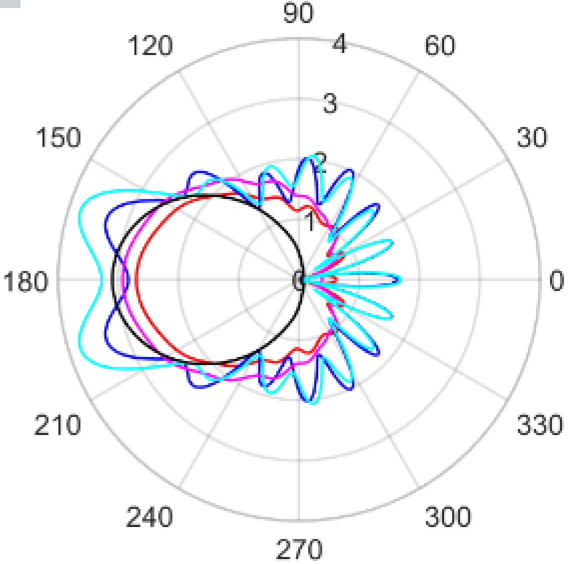
90
120
60
150
30
180
0
210
330
240
300
270
4
3
2
1
0

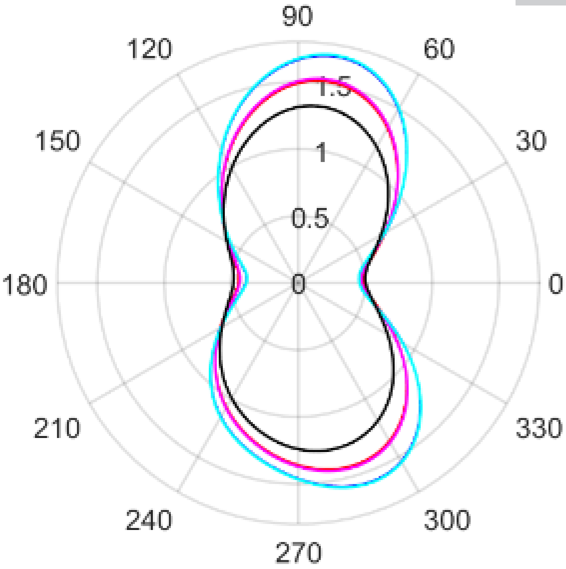

90
120
60
1.5
150
1
30
0.5
180
0
0
210
330
240
300
270

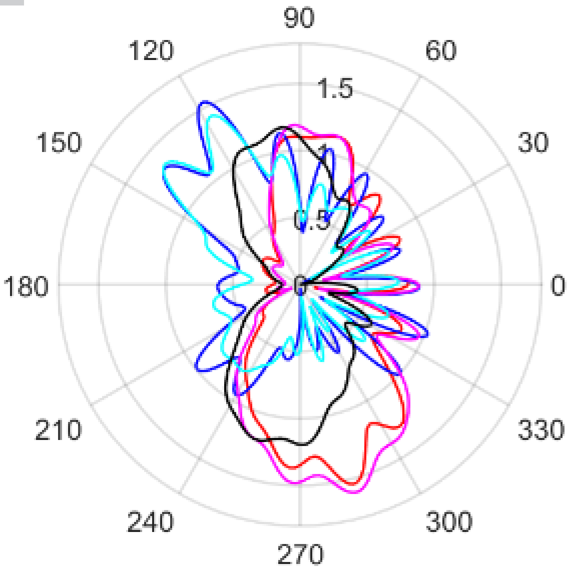

90
120
60
1.5
150
30
1
0.5
180
0
0
210
330
240
300
270

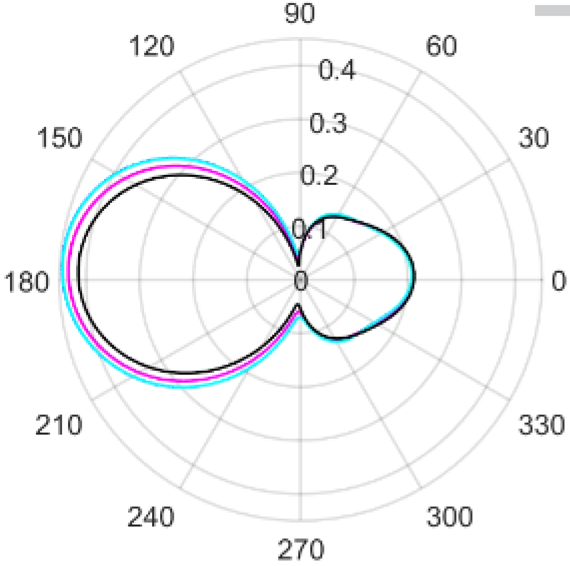
90
120
60
0.4
150
0.3
30
0.2
0.1
180
0
0
210
330
240
300
270

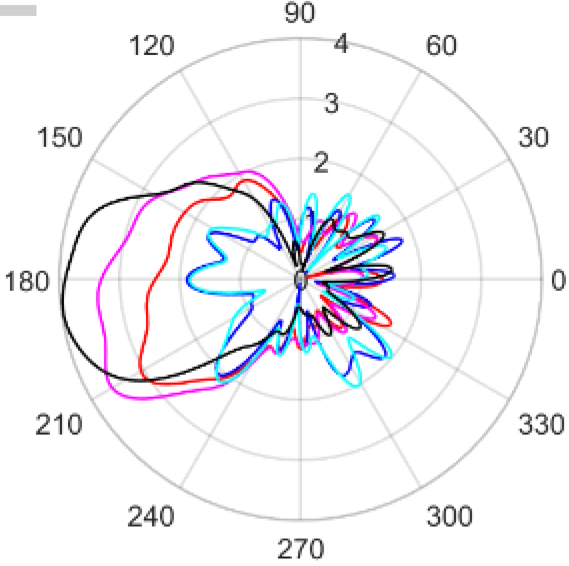
90
4
120
60
3
150
30
2
180
0
0
210
330
240
300
270

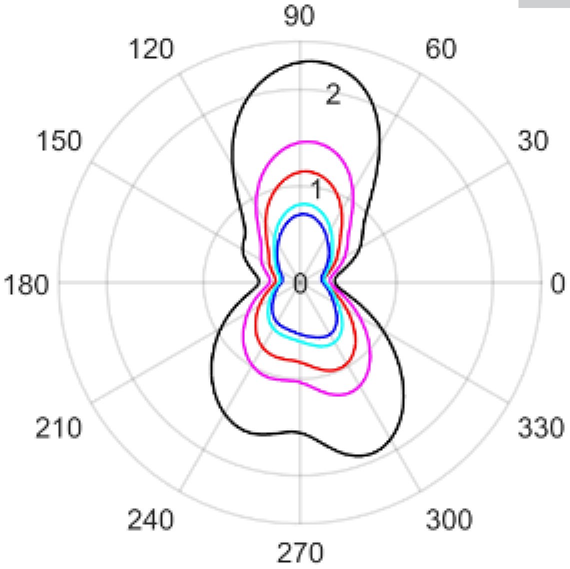
90
120
60
150
30
180
0
210
330
240
300
270
2
1
0

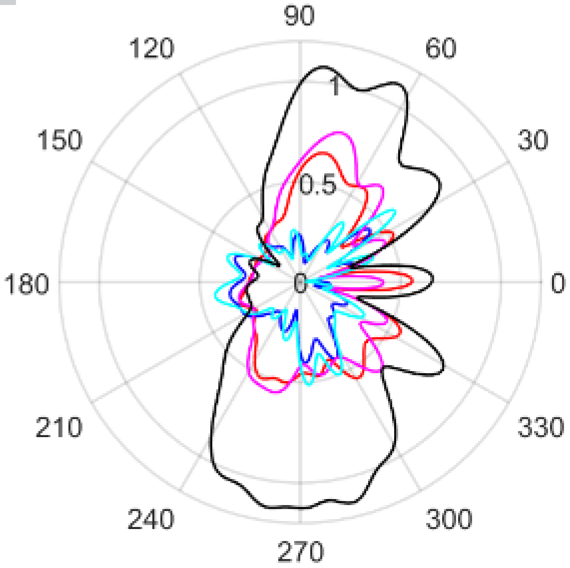
90
120
60
150
30
180
0
210
330
240
300
270
1
0.5
0

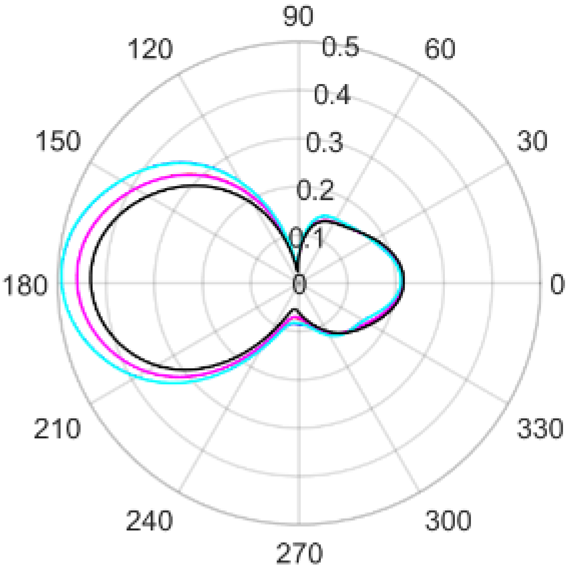
90
120
60
0.5
0.4
0.3
0.2
0.1
0
150
30
180
0
210
330
240
300
270

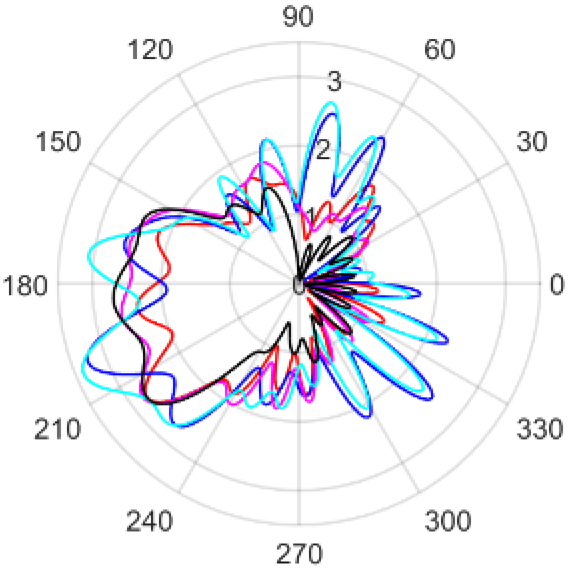
90
120
60
3
150
2
30
1
180
0
0
210
330
240
300
270

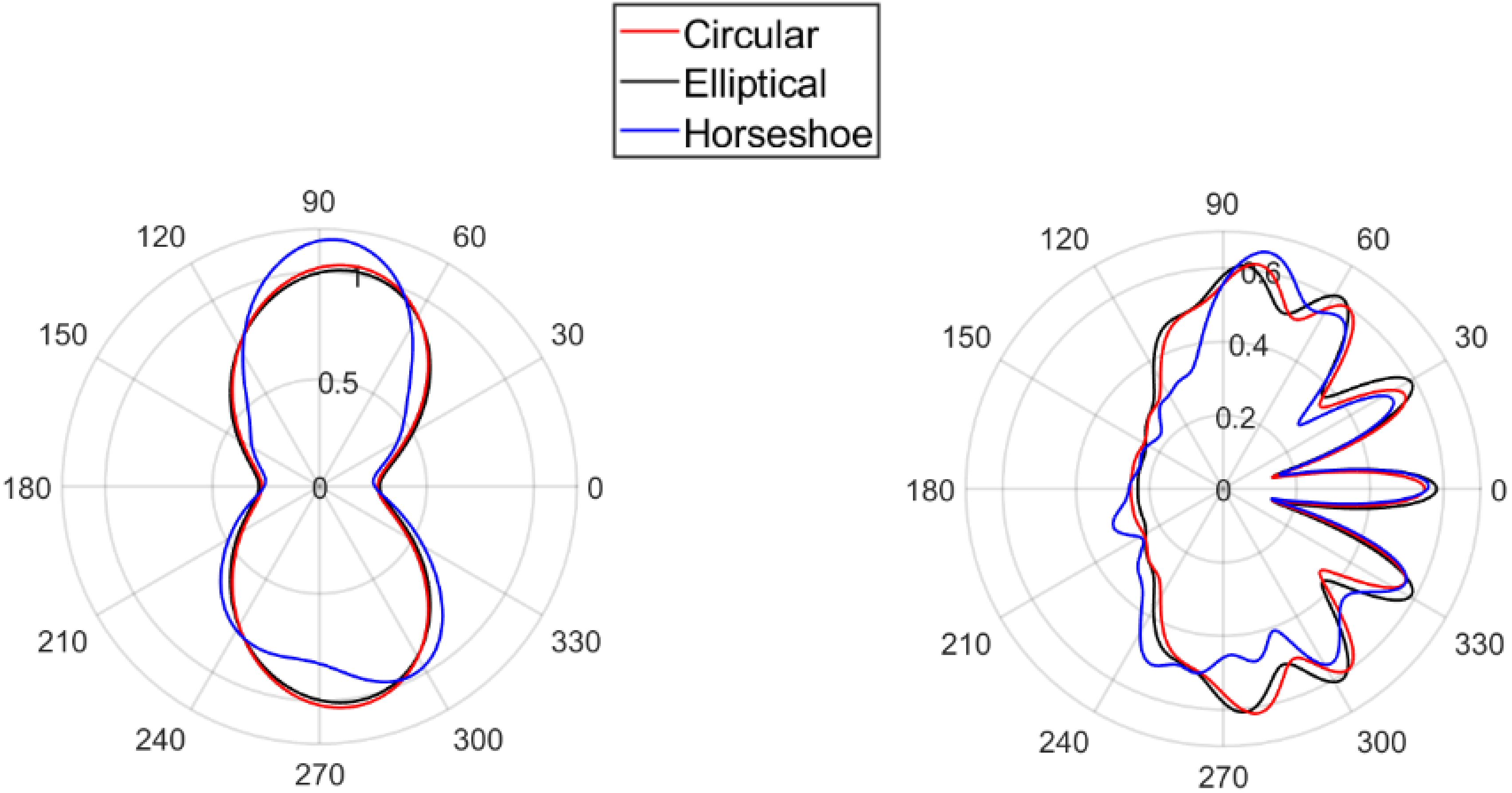
Circular
Elliptical
Horseshoe
90
120
60
150
30
180
0
210
330
240
300
270
0.5
1
0
90
120
60
150
30
180
0
210
330
240
300
270
0.2
0.4
0.6
0

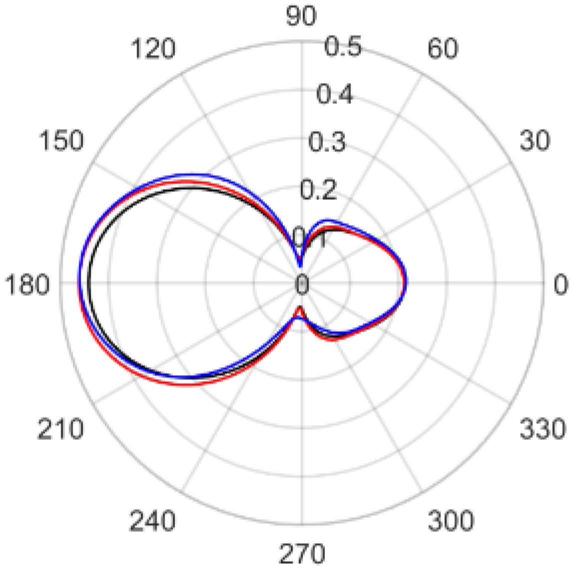
90
120
60
150
30
180
0
210
330
240
300
270
0.5
0.4
0.3
0.2
0.1
0

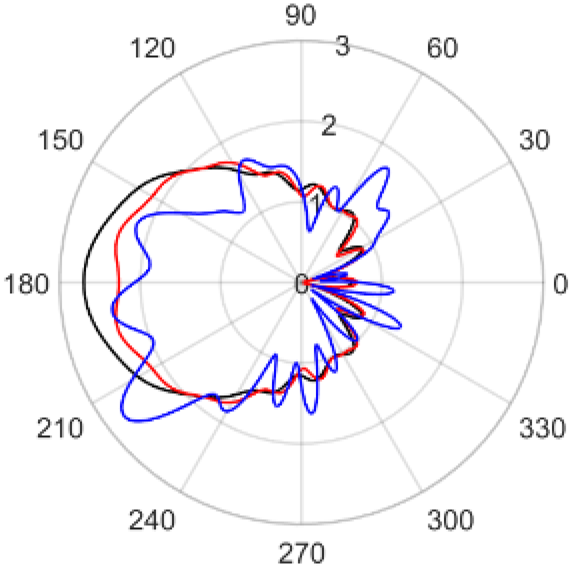
90
120
60
150
30
180
0
210
330
240
300
270
3
2
1
0

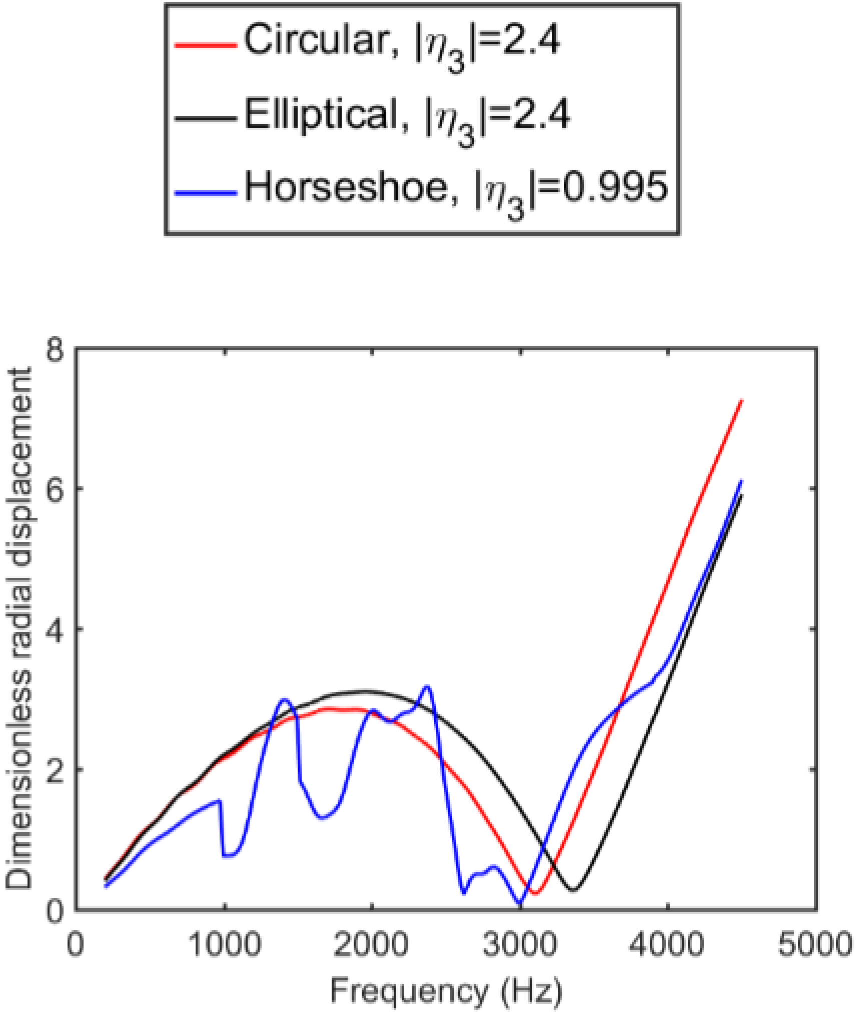
Circular, $|\eta_3|$=2.4
Elliptical, $|\eta_3|$=2.4
Horseshoe, $|\eta_3|$=0.995
Dimensionless radial displacement
0
2
4
6
8
Frequency (Hz)
0
1000
2000
3000
4000
5000

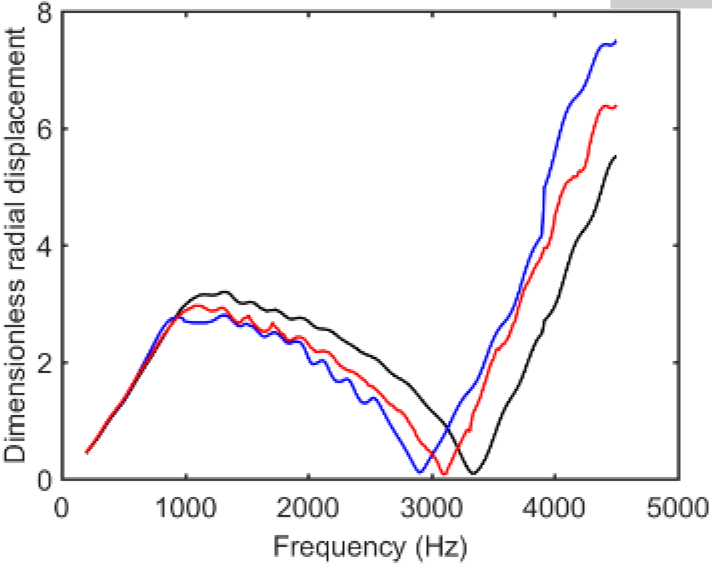
Dimensionless radial displacement
0
2
4
6
8
0
1000
2000
3000
4000
5000
Frequency (Hz)

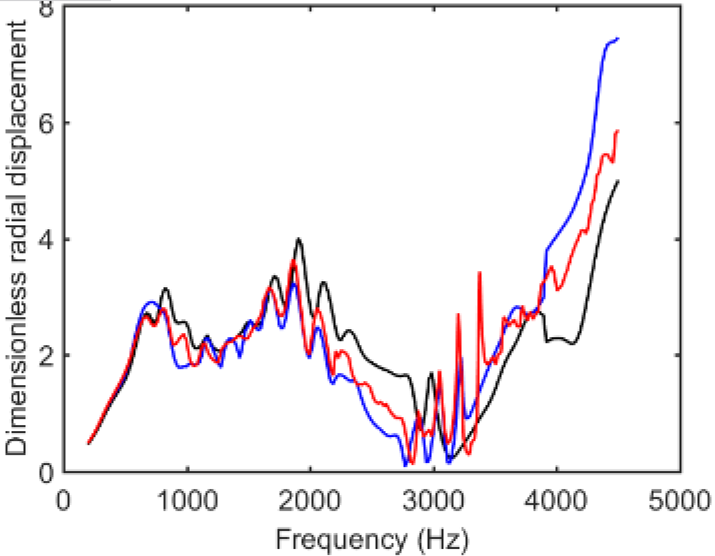
Dimensionless radial displacement
0
2
4
6
8
0
1000
2000
3000
4000
5000
Frequency (Hz)

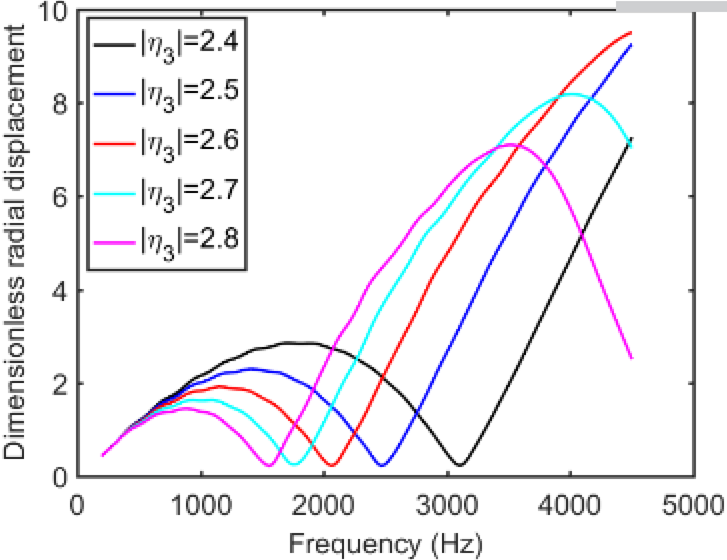
|η_3|=2.4
|η_3|=2.5
|η_3|=2.6
|η_3|=2.7
|η_3|=2.8
Dimensionless radial displacement
0
2
4
6
8
10
0
1000
2000
3000
4000
5000
Frequency (Hz)

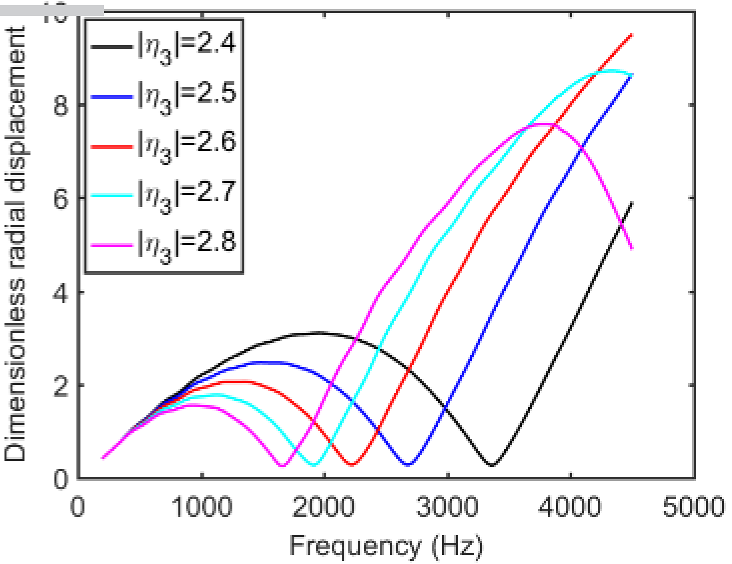
|η_3|=2.4
|η_3|=2.5
|η_3|=2.6
|η_3|=2.7
|η_3|=2.8
Dimensionless radial displacement
0
2
4
6
8
10
0
1000
2000
3000
4000
5000
Frequency (Hz)

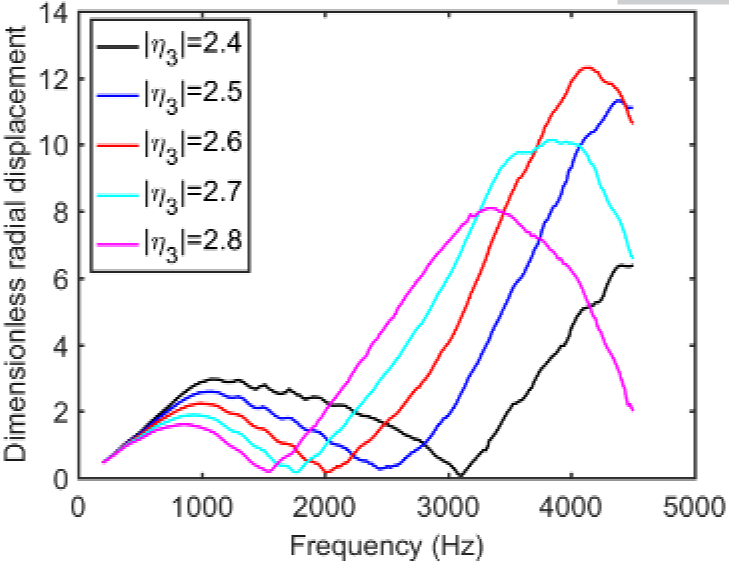
|η_3|=2.4
|η_3|=2.5
|η_3|=2.6
|η_3|=2.7
|η_3|=2.8
Dimensionless radial displacement
Frequency (Hz)
0
2
4
6
8
10
12
14
0
1000
2000
3000
4000
5000

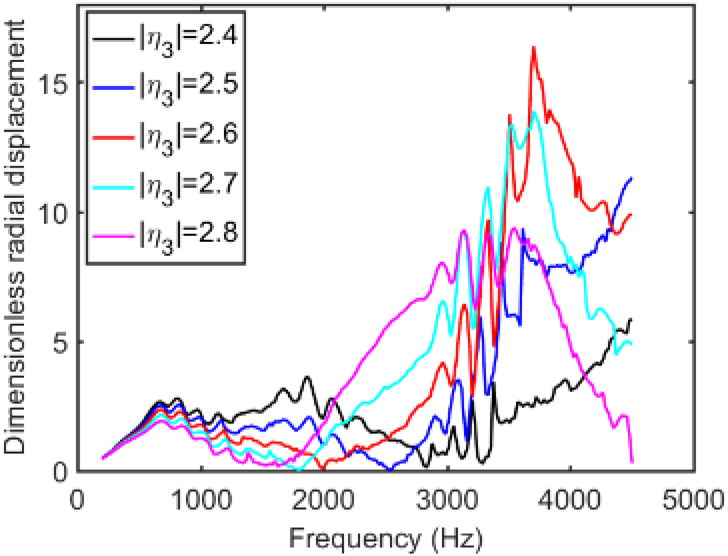
|η_3|=2.4
|η_3|=2.5
|η_3|=2.6
|η_3|=2.7
|η_3|=2.8
Dimensionless radial displacement
Frequency (Hz)
0
5
10
15
0
1000
2000
3000
4000
5000

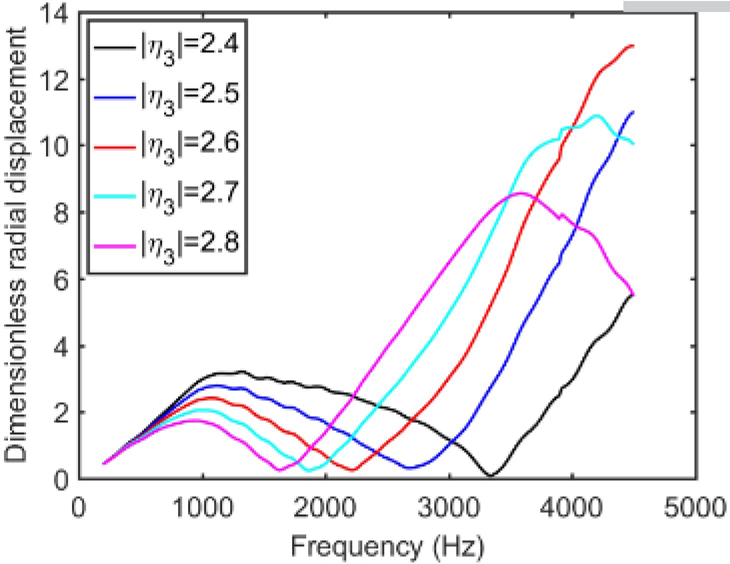
Dimensionless radial displacement
Frequency (Hz)
0
2
4
6
8
10
12
14
0
1000
2000
3000
4000
5000
|η_3|=2.4
|η_3|=2.5
|η_3|=2.6
|η_3|=2.7
|η_3|=2.8

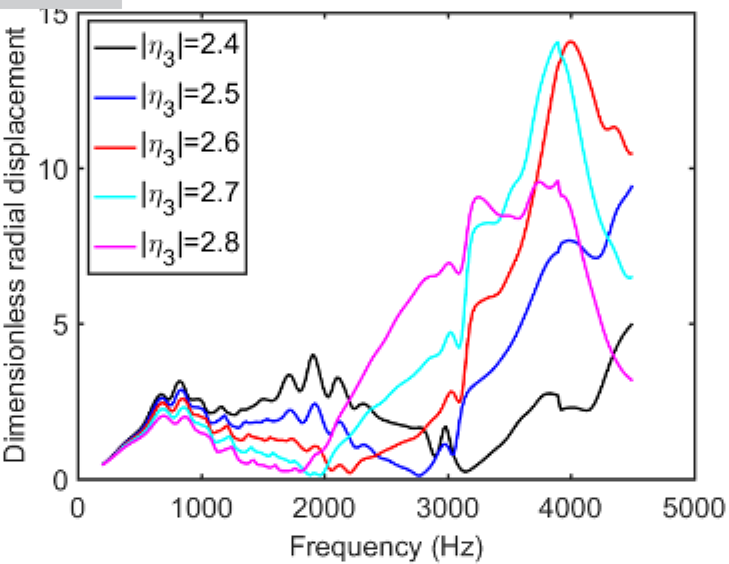
Dimensionless radial displacement
Frequency (Hz)
0
5
10
15
0
1000
2000
3000
4000
5000
|η_3|=2.4
|η_3|=2.5
|η_3|=2.6
|η_3|=2.7
|η_3|=2.8

- -
  fields around an arbitrary shape tunnel

- A multilayered description of the excavation-damaged zone is considered

- Circular, elliptic and horseshoe shapes can be handled for the excavation damaged zone and the tunnel

- Geometrical shapes impact stress and displacement polar diagrams for harmonic regimes

Declaration of interests

☒The authors declare that they have no known competing financial interests or personal relationships that could have appeared to influence the work reported in this paper.

☐The authors declare the following financial interests/personal relationships which may be considered as potential competing interests: